



Towards spaceborne monitoring of localized CO₂ emissions: an instrument concept and first performance assessment

Johan Strandgren¹, David Krutz², Jonas Wilzewski^{1,3}, Carsten Paproth², Ilse Sebastian², Kevin R. Gurney⁴, Jianming Liang⁵, Anke Roiger¹, and André Butz⁶

¹Deutsches Zentrum für Luft- und Raumfahrt, Institut für Physik der Atmosphäre, Oberpfaffenhofen, Germany

²Deutsches Zentrum für Luft- und Raumfahrt, Institut für Optische Sensorsysteme, Berlin-Adlershof, Germany

³Meteorological Institute Munich, Ludwig-Maximilians-Universität, Munich, Germany

⁴School of Informatics, Computing and Cyber Systems, Northern Arizona University, Flagstaff, AZ, USA

⁵School of Life Sciences, Arizona State University, Tempe, AZ, USA

⁶Institut für Umweltphysik, Universität Heidelberg, Heidelberg, Germany

Correspondence: Johan Strandgren (johan.strandgren@dlr.de)

Received: 31 October 2019 – Discussion started: 16 January 2020

Revised: 6 April 2020 – Accepted: 17 April 2020 – Published: 3 June 2020

Abstract. The UNFCCC (United Nations Framework Convention on Climate Change) requires the nations of the world to report their carbon dioxide (CO₂) emissions. The independent verification of these reported emissions is a cornerstone for advancing towards the emission accounting and reduction measures agreed upon in the Paris Agreement. In this paper, we present the concept and first performance assessment of a compact spaceborne imaging spectrometer with a spatial resolution of 50 × 50 m² that could contribute to the “monitoring, verification and reporting” (MVR) of CO₂ emissions worldwide. CO₂ emissions from medium-sized power plants (1–10 MtCO₂ yr⁻¹), currently not targeted by other spaceborne missions, represent a significant part of the global CO₂ emission budget. In this paper we show that the proposed instrument concept is able to resolve emission plumes from such localized sources as a first step towards corresponding CO₂ flux estimates.

Through radiative transfer simulations, including a realistic instrument noise model and a global trial ensemble covering various geophysical scenarios, it is shown that an instrument noise error of 1.1 ppm (1σ) can be achieved for the retrieval of the column-averaged dry-air mole fraction of CO₂ (XCO₂). Despite a limited amount of information from a single spectral window and a relatively coarse spectral resolution, scattering by atmospheric aerosol and cirrus can be partly accounted for in the XCO₂ retrieval, with deviations

of at most 4.0 ppm from the true abundance for two-thirds of the scenes in the global trial ensemble.

We further simulate the ability of the proposed instrument concept to observe CO₂ plumes from single power plants in an urban area using high-resolution CO₂ emission and surface albedo data for the city of Indianapolis. Given the preliminary instrument design and the corresponding instrument noise error, emission plumes from point sources with an emission rate down to the order of 0.3 MtCO₂ yr⁻¹ can be resolved, i.e., well below the target source strength of 1 MtCO₂ yr⁻¹. This leaves a significant margin for additional error sources, like scattering particles and complex meteorology, and shows the potential for subsequent CO₂ flux estimates with the proposed instrument concept.

1 Introduction

Despite the broad consensus on the negative long-term effects of carbon dioxide (CO₂) emissions and the efforts to reduce these emissions, the atmospheric CO₂ concentrations continue to rise. During the course of 2018, the average CO₂ concentration increased from 407 to 410 ppm at the Mauna Loa observatory, representing the fourth-highest annual growth ever recorded at that observatory (NOAA, 2019). CO₂ emissions from localized point sources represent a large fraction of the CO₂ emitted into the atmo-

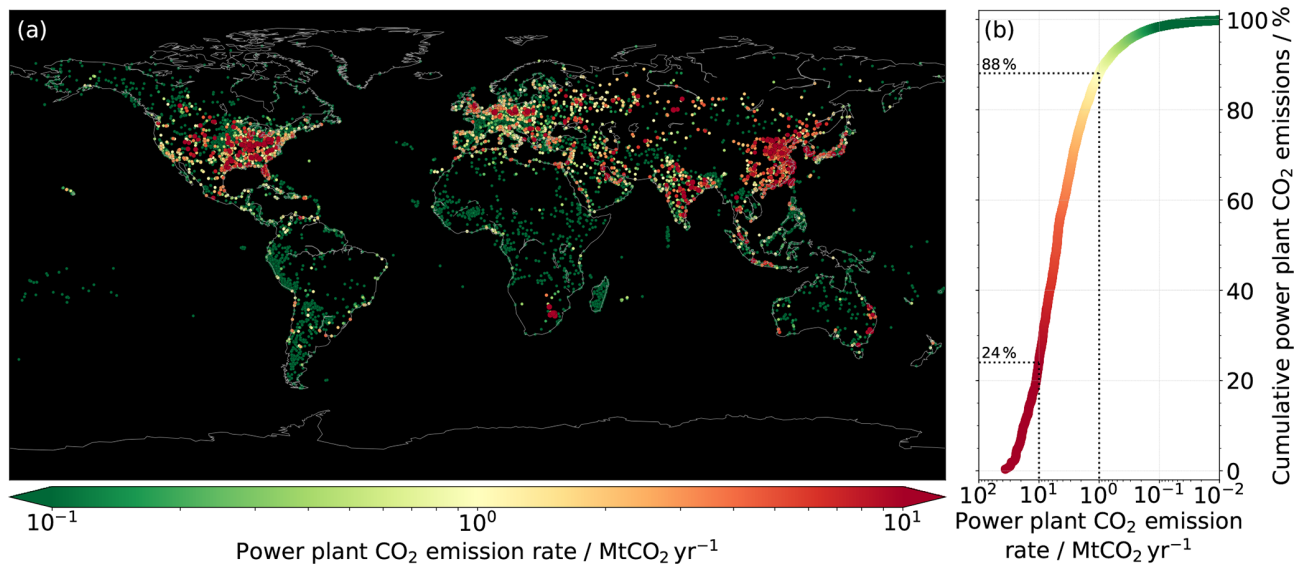


Figure 1. (a) Geographical distribution of reported and estimated annual CO₂ emissions from power plants worldwide for the year 2009, as provided by the CARMA v3.0 database. (b) Corresponding cumulative distribution showing the fraction of the power plant emission total (9.9 GtCO₂ yr⁻¹) that power plants with a source strength greater than X MtCO₂ yr⁻¹ make up. This should be understood as the fraction of the power plant CO₂ emission total that can theoretically be observed by an instrument with a given sensitivity. For visualization purposes, the marker sizes in (a) are scaled according to the respective emission rates.

sphere. The International Energy Agency (IEA) recently reported that emissions from coal-fired power plants exceeded 10 GtCO₂ yr⁻¹ for the first time in 2018, hence accounting for approximately 30 % of the global CO₂ emissions (IEA, 2019), mainly due to the continued growth of coal use in Asia and other emerging economies. Figure 1 depicts the global distribution of reported and estimated annual CO₂ emissions from power plants for the year 2009, as provided by the CARMA (Carbon Monitoring for Action) v3.0 database (Wheeler and Ummel, 2008; Ummel, 2012), together with the corresponding cumulative distribution of the power plant emissions. The emission total from 16 898 individual power plants, where exact or approximate coordinates are available, adds up to 9.9 GtCO₂ yr⁻¹. A large fraction of power plant emissions originates from a relatively small number of large to medium-sized power plants. The CARMA data show that 153 large power plants (> 10 MtCO₂ yr⁻¹) accounted for 24 % of the total annual power plant CO₂ emissions, whereas 2111 large and medium-sized power plants (> 1 MtCO₂ yr⁻¹) accounted for as much as 88 % of the power plant CO₂ emission budget, clearly demonstrating the significant contribution from medium-sized power plants (1–10 MtCO₂ yr⁻¹) to the global CO₂ emission budget.

To advance towards emission accounting and reduction measures, agreed upon in the Paris Agreement in force since 2016, the independent verification of reported emissions is of high importance. To this end, spaceborne instruments provide a suitable platform with which continuous long-term measurements can potentially be combined with near-global coverage with no geopolitical boundaries.

Most of the currently operating, planned and proposed instruments for passive CO₂ observations from space measure the reflected shortwave infrared (SWIR) solar radiation in several spectral windows covering the oxygen A (O₂ A) band near 750 nm as well as the weak and strong CO₂ absorption bands near 1600 and 2000 nm, respectively, e.g., GOSAT (Greenhouse Gases Observing Satellite; Kuze et al., 2009, 2016), OCO-2 (Orbiting Carbon Observatory-2; Crisp et al., 2004, 2017), TanSat (Liu et al., 2018), GOSAT-2 (Nakajima et al., 2012), OCO-3 (Eldering et al., 2019), MicroCarb (Buil et al., 2011), GeoCarb (Moore et al., 2018), CarbonSat (Bovensmann et al., 2010; Buchwitz et al., 2013) and G3E (Geostationary Emission Explorer for Europe; Butz et al., 2015). These instruments and instrument concepts further rely on a comparatively high spectral resolution on the order of approximately 0.05–0.3 nm, representing resolving powers (ratio of wavelength over the full-width half-maximum of the instrument spectral response function) ranging from approximately 3600 for the strong CO₂ absorption bands near 2000 nm for CarbonSat (Buchwitz et al., 2013) up to > 20 000 for the OCO and GOSAT instruments. Such advanced instruments, like GOSAT and OCO-2 that have been operating since 2009 and 2014, respectively, generally target an accuracy and coverage sufficient to study the natural CO₂ cycle on a regional to continental scale (e.g., Guerlet et al., 2013; Maksyutov et al., 2013; Parazoo et al., 2013; Eldering et al., 2017; Chatterjee et al., 2017; Liu et al., 2017) but have also been used to observe and quantify CO₂ gradients on the regional scale caused by anthropogenic CO₂ emissions in urban areas (Kort et al., 2012; Hakkarainen et al.,

2016; Schwandner et al., 2017; Reuter et al., 2019). OCO-2 data have further been used to observe strong CO₂ plumes from localized natural and anthropogenic CO₂ sources like volcanoes and coal-fired power plants (Nassar et al., 2017; Schwandner et al., 2017; Reuter et al., 2019), demonstrating the capabilities of imaging spectrometers to monitor CO₂ from space. The spatial resolution of OCO-2 and similar instruments like OCO-3, TanSat and the planned Copernicus CO₂ Monitoring mission CO2M (on the order of 2–4 km²) does, however, pose a difficulty for the routine monitoring of localized power plant CO₂ emissions, since the plume is usually only sampled by a handful of pixels in which CO₂ plume enhancements cannot be fully separated from the background, making quantitative CO₂ emission rate estimates difficult and vulnerable to cloud contamination and instrument noise propagating into CO₂ retrieval errors. For this reason CO2M will target isolated large power plants ($\gtrsim 10 \text{ MtCO}_2 \text{ yr}^{-1}$) and large urban agglomerations (\gtrsim Berlin) (Kuhlmann et al., 2019), and thus a large fraction of the emission total will be missed.

To contribute to closing this gap and expanding on future CO₂ monitoring from space, we present the concept and a first performance assessment of a spaceborne imaging spectrometer that could be deployed for the dedicated monitoring of localized CO₂ emissions. By targeting power plants with an annual emission rate down to approximately $1 \text{ MtCO}_2 \text{ yr}^{-1}$, a substantial fraction of the CO₂ emissions from power plants and hence a significant part of the global man-made CO₂ emission budget in total could be resolved (given global coverage through a fleet of instruments). As shown in Fig. 1, it is of key importance to also cover medium-sized power plants ($1\text{--}10 \text{ MtCO}_2 \text{ yr}^{-1}$) as they alone contributed to approximately 64 % of the CO₂ emissions from power plants in 2009 according to the CARMA v3.0 data. To achieve this, the proposed instrument has an envisaged spatial resolution of $50 \times 50 \text{ m}^2$. With such a high spatial resolution and large amount of ground pixels per unit area, averaging plume enhancements and background concentration fields is avoided. This leads to an enhanced contrast compared to a coarser spatial resolution. To increase the number of collected photons and hence the signal-to-noise ratio (SNR) and relative precision of the CO₂ concentration retrievals, such a high spatial resolution has to be compensated for with a rather coarse spectral resolution. To further compensate for the limited spatial coverage of a single instrument, a comparatively compact and low-cost instrument design is an important aspect, as it would allow for a fleet of instruments to be deployed, increasing the spatial coverage.

Wilzewski et al. (2020) recently demonstrated that atmospheric CO₂ concentrations can be retrieved with an accuracy $< 1 \%$ using such a comparatively simple spectral setup with one single spectral window and a relatively coarse spectral resolution of approximately 1.3–1.4 nm (resolving power of 1400–1600). Thompson et al. (2016) demonstrated the abil-

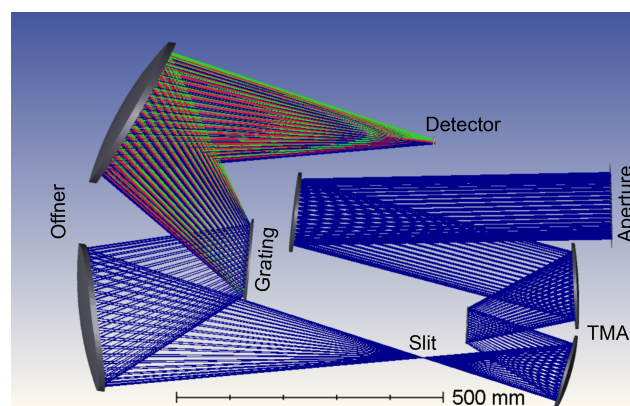


Figure 2. Ray-tracing diagram of the preliminary optical design assuming a three-mirror anastigmat (TMA) telescope combined with an Offner-type spectrometer.

ity to resolve and quantify methane (CH₄) plumes, which pose a similar remote sensing challenge as CO₂, using data from the spaceborne Hyperion imaging spectrometer with a spectral and spatial resolution of 10 nm (resolving power around 230) and 30 m, respectively. The observation of emission plumes, from plume detection to enhancement quantification and flux estimation, using imaging spectroscopy with a single narrow spectral window and a spectral resolution as coarse as 5 to 10 nm (resolving power around 200–500) has further been repeatedly demonstrated using airborne imaging spectroscopy data for both CO₂ (Dennison et al., 2013; Thorpe et al., 2017) and CH₄ (Thorpe et al., 2014; Thompson et al., 2015; Thorpe et al., 2016, 2017; Jongaramrungruang et al., 2019). For an airborne instrument primarily dedicated to the quantitative imaging of CH₄, but also CO₂ plumes, Thorpe et al. (2016) proposed a single spectral window and a spectral resolution of 1.0 nm (resolving power around 2000–2400), again coarse enough to reach a spatial resolution on the order of 10–100 m. The commercial instrument GHGSat-D operated by the Canadian company GHGSat Inc. was launched in 2016 as a demonstrator for a satellite constellation concept targeting the detection of CH₄ plumes from individual point sources within selected $\approx 10 \times 10 \text{ km}^2$ target regions at a spectral and spatial resolution of 0.1 nm (resolving power around 16 000) and 50 m, respectively (Varon et al., 2018). Varon et al. (2019) recently showed how anomalously large CH₄ point sources can be discovered with GHGSat-D observations.

Given the results from previous studies and the technology at hand, we are confident that the proposed instrument concept presented here could be realized and that it would be an important complement to the fleet of current and planned spaceborne CO₂ instruments, allowing for the routine quantitative monitoring of CO₂ emissions from large and medium-sized power plants. The proposed instrument concept would also serve as a good complement and companion to CO2M

by also targeting medium-sized power plants and providing high-resolution images with finer CO₂ plume structures. The added value of such an instrument would be of interest both in terms of advancing science and providing independent emission estimates that could be used to verify reported CO₂ emission rates at the facility level and inform policy makers on the progress of reducing man-made CO₂ emissions. The proposed instrument concept is described in Sect. 2, followed by a description of the instrument noise model in Sect. 3. A global performance assessment addressing instrument noise and the errors introduced by atmospheric aerosol is presented in Sect. 4. The ability to resolve single CO₂ emission plumes at an urban scale is further simulated in Sect. 5. A short summary and our concluding remarks are finally presented in Sect. 6.

2 Mission and instrument concept

The instrument concept presented in this paper is based on a spaceborne push-broom imaging grating spectrometer measuring spectra of reflected solar radiation in one single SWIR spectral window, from which the column-averaged dry-air mole fraction of CO₂ (XCO₂) can be retrieved. With an expected instrument mass of approximately 90 kg, it is suitable for deployment on small satellite buses. Since the proposed instrument targets the quantification of localized CO₂ emissions from, e.g., coal-fired power plants, a high spatial resolution of 50 × 50 m² is envisaged. The instrument is designed to fly in a sun-synchronous orbit at an altitude of 600 km and a local equatorial crossing time at 13:00 LT. This orbit is chosen in order to have a well-developed boundary layer at overpass together with good radiometric performance (high SNR).

The preliminary optical design assumes a circular aperture (15 cm in diameter) and is based on a three-mirror anastigmat (TMA) telescope, combined with an Offner-type spectrometer, as shown in Fig. 2. The optic system relies on metal-based mirrors and is designed as an athermal configuration for a wide temperature range onboard the satellite. The three mirrors of the TMA are standard aspheres aligned on a single optical axis. The efficiency of the optical bench (throughput), including transmittance and grating efficiency, is estimated to 0.48, and the f number (f_{num}), equal to the ratio of focal length to aperture diameter, amounts to 2.4. The dispersed electromagnetic radiation is focused onto a two-dimensional array detector that captures the spatial across-track dimension and the spectral dimension of the incoming radiation. A detector with a pixel area of 900 μm² and a quantum efficiency of 0.8 is assumed for this study. The quantum efficiency depends on the wavelength but is for now assumed constant for both spectral windows. These values are in line with typical values for a state-of-the-art detector.

In order to reach a sufficient SNR, the proposed spatial resolution only allows for a relatively coarse spectral res-

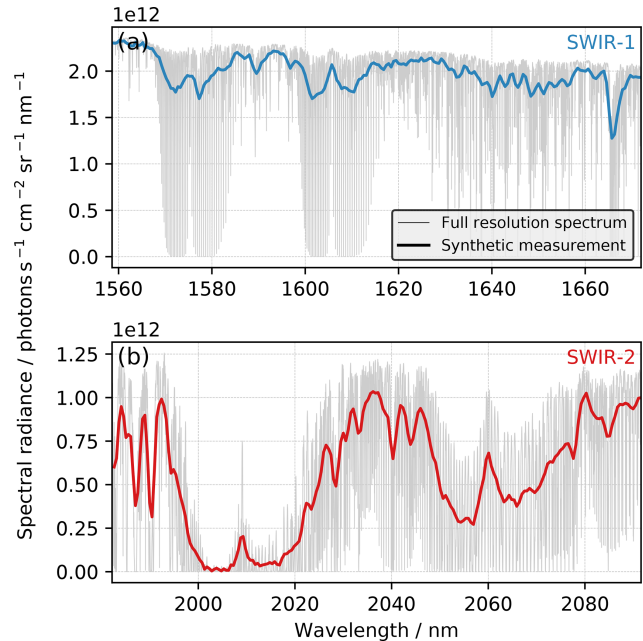


Figure 3. Simulated synthetic measurements of spectral radiances for the two spectral setups near 1600 nm (SWIR-1) (a) and 2000 nm (SWIR-2) (b) for our reference scene with surface albedo 0.1 and an SZA of 70°. Thin grey lines show corresponding spectral radiances at 0.003 nm spectral resolution.

olution. Wilzewski et al. (2020) used spectrally degraded GOSAT soundings to demonstrate the capability of retrieving XCO₂ from a single spectral window at such a coarse spectral resolution using a spectral setup (in terms of spectral range, resolution and oversampling ratio) compact enough to fit onto 256 detector pixels. They evaluate two alternative spectral setups covering the spectral ranges 1559–1672 nm (hereafter also referred to as SWIR-1) and 1982–2092 nm (hereafter also referred to as SWIR-2) with a spectral resolution (full-width half-maximum – FWHM – of the instrument spectral response function) of 1.37 and 1.29 nm, respectively, and an oversampling ratio of 3. The resolving power of the SWIR-1 and SWIR-2 setups amounts to approximately 1200 and 1600, respectively. For optics design reasons, we use a spectral oversampling ratio of 2.5 in this study, resulting in a spectral sampling distance of 0.55 and 0.52 nm for SWIR-1 and SWIR-2, respectively. Simulated synthetic measurements of spectral radiances for the two prospective spectral setups are shown in Fig. 3, assuming a Gaussian instrument response function with an FWHM of 1.37 and 1.29 nm, respectively, as proposed by Wilzewski et al. (2020). The SWIR-1 window (Fig. 3a) exhibits two weak CO₂ absorption bands around 1568–1585 nm and 1598–1615 nm and has the advantage of a stronger top-of-atmosphere (TOA) signal due to higher solar irradiance and surface albedo at these wavelengths. It also allows for the simultaneous retrieval of CH₄ using the CH₄ absorption band near 1666 nm. The SWIR-2

Table 1. Mission and instrument design parameters of the proposed spaceborne CO₂ monitoring instrument concept.

Orbit	600 km, sun-synchronous
Mass	90 kg
Swath	50 km
Spatial resolution	50 × 50 m ²
Spectral range	1559–1672 or 1982–2092 nm
FWHM (2.5 pix)	1.37 or 1.29 nm
Resolving power	1200 or 1600 (–)
Aperture diameter	15.0 cm
<i>f</i> number (<i>f</i> _{num})	2.4 (–)
Optical efficiency (<i>η</i>)	0.48 (–)
Integration time (<i>t</i> _{int})	70 ms
Detector pixel area (<i>A</i> _{det})	900 μm ²
Quantum efficiency (<i>Q</i> _e)	0.8 e [–] photon ^{–1}
Dark current (<i>I</i> _{dc})	1.6 fA pix ^{–1} s ^{–1}
Readout noise	100 e [–]
Quantization noise	40 e [–]

window, on the other hand, exhibits two stronger CO₂ absorption bands around 1995–2035 and 2045–2080 nm and has higher sensitivity to atmospheric aerosol that can potentially be exploited during the XCO₂ retrieval (Wilzewski et al., 2020). Wilzewski et al. (2020) showed similar performance for SWIR-1 and SWIR-2 but suspect SWIR-2 to be the favorable spectral setup given the stronger CO₂ absorption bands, the ability to account for particle scattering and the lower radiance SNR required to reach sufficiently small XCO₂ noise errors. In this paper, we further investigate the performance of the two spectral setups in order to finally conclude which is the more suitable one given the preliminary instrument design and realistic instrument SNR assumed here.

The instrument is designed to have a radiance SNR of 100 at the continuum for a reference scene with a Lambertian surface albedo of 0.1 and solar zenith angle (SZA) of 70°. Given the altitude of 600 km and the corresponding orbital velocity of 7562 ms^{–1}, the instrument traverses along one 50 m ground pixel in 7.2 ms. The number of photons collected over the course of 7.2 ms is, however, not enough to reach an SNR of 100. To increase the SNR, we suggest increasing the integration time to 70 ms. This would normally lead to elongated ground pixels (approx. 50 × 500 m²), but by using forward motion compensation (FMC), the instrument can be periodically altered in the along-track direction such that each ground pixel is sampled for a time period longer than the actual satellite overpass time (see, e.g., Sandau, 2010; Abdollahi et al., 2014). FMC has the evident drawback that the coverage along the satellite track is discontinuous, since no data are sampled when the instrument returns to the starting forward position. A second disadvantage is the geometrical distortion of the ground pixels that increases with the maximum off-nadir angle. The baseline design assumes 1000

measurements to be made in the along-track dimension for each FMC repetition, leading to off-nadir angles up to approximately 20°. Further assuming 1000 detector pixels in the spatial dimension would consequently result in observed tiles on the order of 50 × 50 km².

Table 1 summarizes the preliminary mission concept and instrument design parameters assumed for this study. It should be clear that this is a preliminary baseline design used to demonstrate the CO₂ monitoring abilities and added value of the proposed instrument concept. Alternative instrument designs will be further investigated, and the exact instrument design will most likely be subject to change before the instrument is realized. The continuum SNR for our reference scene should nevertheless remain at roughly 100, ensuring a similar performance as presented in this paper.

3 Instrument noise model

To assess the performance of the proposed instrument concept with respect to retrieving XCO₂ and resolving localized CO₂ emissions, the expected instrument noise levels that accompany the measurements have to be quantified. To this end a numerical instrument noise model that calculates the instrument’s SNR is developed, following a similar approach as, e.g., Bovensmann et al. (2010) and Butz et al. (2015). The SNR is given by

$$SNR = \frac{S}{\sigma_{tot}}, \tag{1}$$

where *S* is the signal, i.e., the number of photons emerging from a 50 × 50 m² ground pixel that generate a charge in the detector, and σ_{tot} is the corresponding instrument noise. The signal *S* is calculated as

$$S = L_{\lambda} \cdot \frac{\pi \cdot A_{det}}{4 \cdot f_{num}^2} \cdot \eta \cdot Q_e \cdot \Delta\lambda \cdot t_{int}, \tag{2}$$

where *L*_λ is the simulated reflected solar spectral radiance at the telescope, *A*_{det} the detector pixel area, *f*_{num} the instrument’s *f* number, *η* the efficiency of the optical bench, *Q*_e the detector’s quantum efficiency, $\Delta\lambda$ the wavelength range covered by a single detector pixel and *t*_{int} the integration time between the detector pixel readouts. Following the thin lens equation (for large distances between a lens and an object) and the magnification formula, the term $\frac{\pi \cdot A_{det}}{4 \cdot f_{num}^2}$ can also be expressed as *A*_{ap} · Ω , where *A*_{ap} is the area of the aperture (= πr^2 with *r* = 7.5 cm) and Ω the instrument’s solid angle, i.e., the squared ratio of the ground sampling distance (50 m) over the orbit altitude (600 km). Apart from *L*_λ that is calculated for each scene using a forward radiative transfer model, all quantities in Eq. (2) and their corresponding values were introduced in Sect. 2.

The total noise σ_{tot} in Eq. (1) accounts for the noise contribution from five separate instrument noise sources:

$$\sigma_{tot} = \sqrt{\sigma_{ss}^2 + \sigma_{bg}^2 + \sigma_{dc}^2 + \sigma_{ro}^2 + \sigma_{qz}^2}, \tag{3}$$

where $\sigma_{ss} = \sqrt{S}$ is the signal shot noise, σ_{bg} is the noise due to thermal background radiation incident on the detector, σ_{dc} is the noise due to dark current in the detector, σ_{ro} is the noise upon detector readout and σ_{qz} the quantization noise that arises when the analog signal is digitized. The thermal background signal per detector pixel is approximated as

$$S_{bg} = A_{det} \cdot Q_e \cdot t_{int} \cdot E_{BB}, \quad (4)$$

where E_{BB} is the thermal black-body irradiance incident on the detector. E_{BB} is determined by integrating the black-body spectral radiance $L_{\lambda, BB}(T_{bg})$ emitted by the background over the detector's cutoff wavelengths λ_1 and λ_2 and hemispheric opening angle,

$$E_{BB} = \pi \int_{\lambda_1}^{\lambda_2} L_{\lambda, BB}(T_{bg}) d\lambda. \quad (5)$$

For this study, detector cutoff wavelengths of 900 and 2500 nm are assumed, and the background temperature T_{bg} is estimated to 200 K. The thermal background noise is then calculated as $\sigma_{bg} = \sqrt{S_{bg}}$. Similarly, the dark current noise is given by $\sigma_{dc} = \sqrt{S_{dc}}$, where $S_{dc} = I_{dc} \cdot t_{int} \cdot Q$ is the per-pixel detector signal due to dark current. While $Q = 6.242 \times 10^{18}$ electrons C^{-1} is constant, the dark current I_{dc} strongly depends on the detector's operating temperature and is estimated to 1.6 fA $\text{pix}^{-1} \text{s}^{-1}$ (assuming 150 K detector temperature), yielding a dark current signal of approximately 10 000 electrons (e^-) per detector pixel and second. Finally, the readout noise (σ_{ro}) and quantization noise (σ_{qz}) are estimated to 100 and 40 e^- , respectively. These noise levels are preliminary estimates used to test and evaluate the instrument concept but are comparable to those of state-of-the-art detectors for space applications.

Figure 4a shows the continuum SNR (calculated with Eqs. 1–5) as a function of the scene brightness for the two prospective spectral setups SWIR-1 and SWIR-2. The scene brightness describes the conversion from incident solar irradiance to reflected solar radiance and is calculated as the product of the surface albedo and the cosine of the SZA divided by π , hence assuming a Lambertian surface. For the reference scene (albedo 0.1, SZA 70°), the continuum SNR is approximately 180 and 100 for SWIR-1 and SWIR-2, respectively. The consistently higher SNR for SWIR-1 compared to SWIR-2 is mainly the result of higher solar radiance (see Fig. 3) and generally higher surface albedo (see, e.g., Fig. 7 in Butz et al., 2009) in SWIR-1. Looking at the individual contributions from the different instrument noise sources in Fig. 4b, it is clear that the readout noise and signal shot noise are the major contributors, whereas the noise arising from quantization errors, dark current and thermal background radiation has a small or even negligible contribution in comparison. The signal shot noise is, however, smaller than the dark current, readout noise and quantization noise inside the CO₂ absorption bands, in which the signal, and hence the signal

shot noise, decreases. Note that all noise terms except for the signal shot noise, σ_{ss} , are constant.

4 Generic performance evaluation

In this section we conduct a first performance evaluation of the proposed instrument concept by assessing the XCO₂ retrieval errors expected on a global scale. Such errors arise due to instrument noise and because of inadequate knowledge about the light path through the atmosphere due to scattering aerosol and cirrus particles. For this purpose we use a global trial ensemble with a large collection of geophysical scenarios with varying atmospheric gas concentrations, meteorological conditions, surface albedo, SZA, and aerosol and cirrus compositions that can be expected to be observed by a polar-orbiting instrument. The same methodology and dataset have been used in several previous studies to assess the greenhouse gas retrieval performance of different satellite instruments (Butz et al., 2009, 2010, 2012, 2015).

The global trial ensemble contains geophysical data representative for the months of January, April, July and October. Atmospheric gas concentrations stem from the Carbon-Tracker model (CO₂ for the year 2010; Peters et al., 2007), the Tracer Model 4 (CH₄ for the year 2006; Meirink et al., 2006) and the ECHAM5-HAM model (H₂O; Stier et al., 2005). Surface albedo data representative for the SWIR-1 and SWIR-2 windows stem from the MODIS (Moderate Resolution Imaging Spectroradiometer) MCD43A4 product (Schaaf et al., 2002). Aerosol optical properties are calculated (assuming Mie scattering) for an aerosol size distribution superimposed from seven lognormal size distributions and five chemical types at 19 vertical layers, as provided by the ECHAM5-HAM model (Stier et al., 2005). Cirrus optical properties are calculated for randomly oriented hexagonal columns and plates following the ray-tracing model of Hess and Wiegner (1994) and Hess et al. (1998). In total the global trial ensemble consists of approximately 10 000 scenes with XCO₂ ranging from 340 to 400 ppm with an average of 382 ppm, albedo ranging from 0 to 0.7 with an average of 0.13 (SWIR-2 window), aerosol optical thickness (AOT) ranging from 0 to 1.0 with an average of 0.05 (SWIR-2 window) and cirrus optical thickness (COT) ranging from 0 to 0.8 with an average of 0.13 (SWIR-2 window). Thus, the global trial ensemble contains challenging scenes with scattering loads that would be filtered out by current satellite retrievals, such as those applied to OCO-2 and GOSAT data, which typically screen scenes with scattering optical thickness greater than 0.3 (at the O₂ A band around 760 nm). All data in the global trial ensemble are re-gridded to a spatial resolution of approximately 2.8° × 2.8°. This is, of course, much coarser than the envisaged 50 × 50 m², but for investigating the propagation of instrument noise into the target quantity XCO₂ on a global scale, this dataset serves its pur-

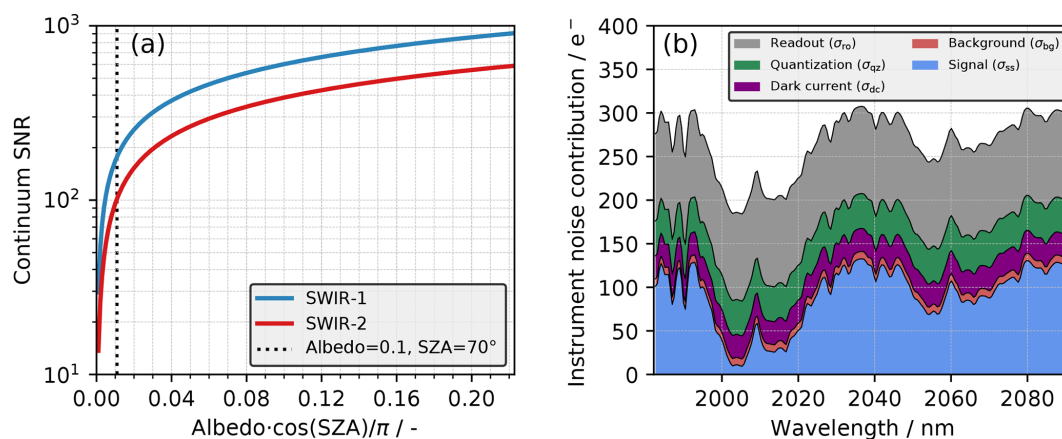


Figure 4. (a) Continuum SNR as a function of scene brightness ($\text{Albedo} \cdot \cos(\text{SZA}) / \pi$) for the SWIR-1 and SWIR-2 spectral setups, with the dotted line indicating the brightness of our reference scene. The highest scene brightness (approx. 0.22) represents a bright scene with an albedo of 0.7 and an SZA of 0°. (b) Instrument noise contributions for a simulated SWIR-2 spectrum.

pose. See previous studies (e.g., Butz et al., 2009, 2010) for further details on the content of the global trial ensemble.

The geophysical data for each scene are fed to the radiative transfer software RemoTeC (Butz et al., 2011; Schepers et al., 2014) in order to simulate corresponding synthetic measurements. The measurement noise is calculated by propagating the instrument's SNR (Sect. 3) into a statistical error estimate according to the rules of Gaussian error propagation (Rodgers, 2000). Simulations are conducted globally for the 16th day of each of the four months January, April, July and October, hence covering SZA conditions ranging from 0 to 86°.

By retrieving XCO₂ from the simulated synthetic spectra, the range of XCO₂ retrieval errors that can be expected with the proposed instrument concept can be estimated, as can the ability to account for atmospheric aerosol. The RemoTeC retrieval algorithm (e.g., Butz et al., 2011) is based on a Phillips–Tikhonov regularization scheme (Phillips, 1962; Tikhonov, 1963) that uses the first-order difference operator as a side constraint to retrieve the CO₂ partial column profiles, from which XCO₂ can be determined. Additional retrieval parameters are the total column concentrations of H₂O and CH₄ (only for SWIR-1), surface albedo (as a second-order polynomial), spectral shift, solar shift, and possibly information on scattering aerosol. Here we assume knowledge about the air mass (needed to calculate XCO₂), but in reality meteorological and topography data would be required to estimate the air mass.

4.1 Instrument-noise-induced XCO₂ errors

In a first step, we assess XCO₂ retrieval errors that are induced by instrument noise. To this end, for now, we neglect scattering by aerosol and cirrus. These so-called non-scattering simulations assume no scattering particles to be present in the atmosphere and simply compute the transmit-

tance along the geometric light path (Rayleigh scattering is included).

Figure 5a shows the cumulative distribution of the random XCO₂ noise error, i.e., the instrument noise propagated into XCO₂ uncertainties via Gaussian error propagation. Furthermore, Fig. 5b shows the XCO₂ noise error for each simulated scene as a function of the corresponding scene brightness. The noise errors are significantly smaller for the SWIR-2 setup (red) when using the proposed integration time t_{int} of 70 ms. The red dashed lines in Fig. 5b show that on average 68 % and 95 % (1 σ and 2 σ , respectively) of the retrievals have noise errors of less than approximately 1.1 and 2.0 ppm, respectively. For the SWIR-1 setup (blue), the corresponding numbers are 2.9 and 5.0 ppm. For the SWIR-2 setup, only retrievals over scenes that are darker than our reference scene (albedo 0.1, SZA 70°) are expected to have instrument-noise-induced errors larger than approximately 2 ppm. For comparison and as a reference, we also investigate how much the integration time has to be increased for the SWIR-1 setup in order to reach an SNR sufficient to yield XCO₂ noise errors comparable to those obtained with the SWIR-2 setup. We find that with the preliminary instrument design assumed here, the integration time has to be increased to at least 350 ms (i.e., by a factor of 5) for SWIR-1 (grey) in order to reach a similar performance.

Despite the advantage of being able to retrieve XCH₄ alongside XCO₂ using the SWIR-1 setup, the much longer integration time required to reach sufficiently low CO₂ noise errors is not feasible for the purpose of the proposed instrument concept. Hence, we conclude that the SWIR-2 setup is superior for the passive satellite-based CO₂ monitoring instrument proposed in this paper. Consequently, the remainder of this paper is limited to the SWIR-2 setup, covering the spectral range 1982–2092 nm with a spectral resolution (FWHM) of 1.29 nm, resolving power around 1600 and a spectral sampling distance of 0.52 nm.

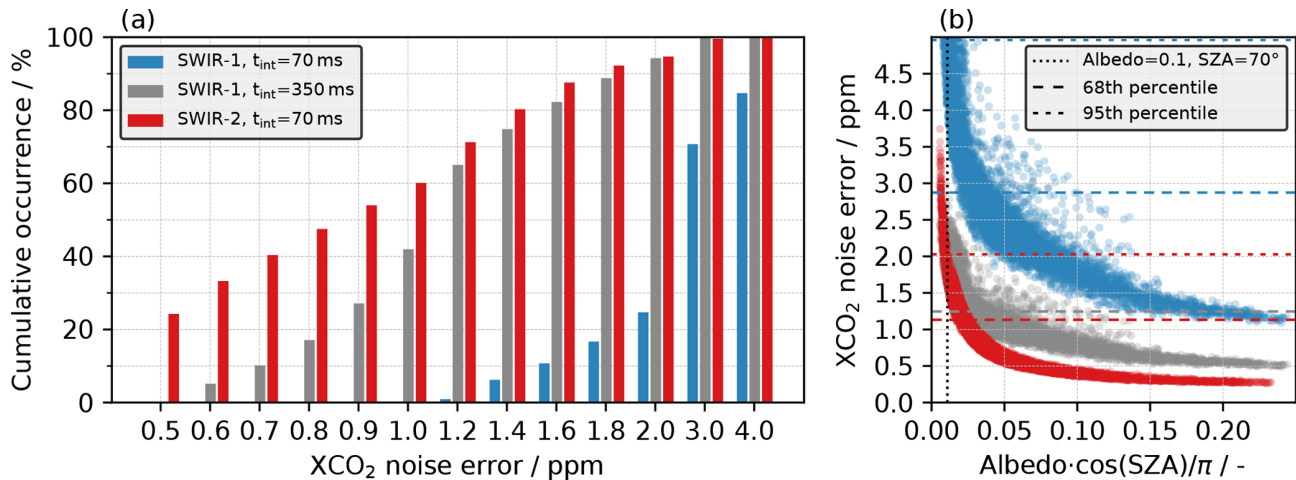


Figure 5. (a) Cumulative distribution of the estimated XCO₂ noise errors arising from instrument noise for all scenes in the global ensemble. (b) XCO₂ noise errors as a function of surface brightness, with the dotted line indicating our reference scene and the dashed lines indicating the 68th and 95th percentiles of the XCO₂ noise errors for the different spectral setups. Note that the red and grey lines for the 95th percentile overlap at 2.03 ppm. Marker colors in (b) correspond to those in (a). Both panels show the results for the SWIR-1 (blue) and SWIR-2 (red) setups as well as for an alternative SWIR-1 (grey) setup for comparison (see the text for details).

4.2 Aerosol-induced XCO₂ errors

Atmospheric aerosol and cirrus particles modify the light path of the reflected solar radiation to a certain degree, depending on the particle abundance, optical properties, height and surface albedo. Consequently, this can cause large errors in the retrieved XCO₂ if the effect of CO₂ absorption and particle scattering on the measured reflected solar radiation cannot be adequately separated during the retrieval process. In this section the ability to account for atmospheric aerosol and cirrus during the retrieval is investigated by including scattering by atmospheric particles in the simulation of the synthetic measurements and in the corresponding XCO₂ retrievals. This is done by using a more complex forward model and representation of the aerosol and cirrus particles when simulating the spectra, as well as a comparatively simple representation and forward model for the corresponding retrievals. More precisely, the full physical representation of the vertical profiles of hexagonal cirrus particles and spherical aerosol particles of the five chemical types characterized by the seven lognormal size distributions with known microphysical properties for each aerosol and cirrus particle type is used when simulating the synthetic measurement for each scene in the global trial ensemble. In contrast, only three aerosol parameters are fitted during the corresponding retrieval: the total column number density, the size parameter of a single-mode power-law size distribution and the center height of a Gaussian height distribution. Such differences in the aerosol and cirrus representation lead to forward model errors that, alongside the instrument-noise-induced errors, propagate into the retrieved quantity XCO₂. Previous studies have shown that this approach gives a good approximation of

how well a satellite sensor can account for scattering by atmospheric aerosol while retrieving target gas concentrations (e.g., Butz et al., 2009, 2010).

Figure 6a shows the difference between the XCO₂ retrieved (“retr”) from the synthetic measurements and the corresponding “true” XCO₂ used as input to simulate these synthetic measurements. This deviation from the truth contains information on both random instrument noise error (Sect. 4.1) and systematic errors arising from insufficient modeling of the aerosol and cirrus properties. For comparison, Fig. 6b shows the corresponding results achieved when using a non-scattering retrieval, i.e., when the scattering by atmospheric aerosol and cirrus, now present in the atmosphere and the simulated synthetic spectra, is neglected (similar to Sect. 4.1). The retrieval errors are strongly reduced when the RemoTeC retrieval algorithm accounts for the scattering by atmospheric aerosol. When scattering is considered, half of the XCO₂ retrievals deviate from the true abundance by less than 2.5 ppm, while two-thirds of the retrievals deviate by less than 4 ppm (approx. 1%), with no clear error correlation with the optical thickness of the scattering particles. For the non-scattering retrieval, the corresponding numbers are 16 and 28 ppm, with a mean bias of −25 ppm that increases with optical thickness, exposing the necessity of accounting for atmospheric aerosol and cirrus when retrieving the XCO₂.

Scattering particles can modify the light path and hence the XCO₂ retrieval in primarily two ways. Firstly, an elevated layer of aerosol or cirrus will scatter parts of the incoming solar radiation towards the observing sensor at a higher altitude compared to the Earth’s surface, leading to a reduced light path. Secondly, aerosol and cirrus will extend the light

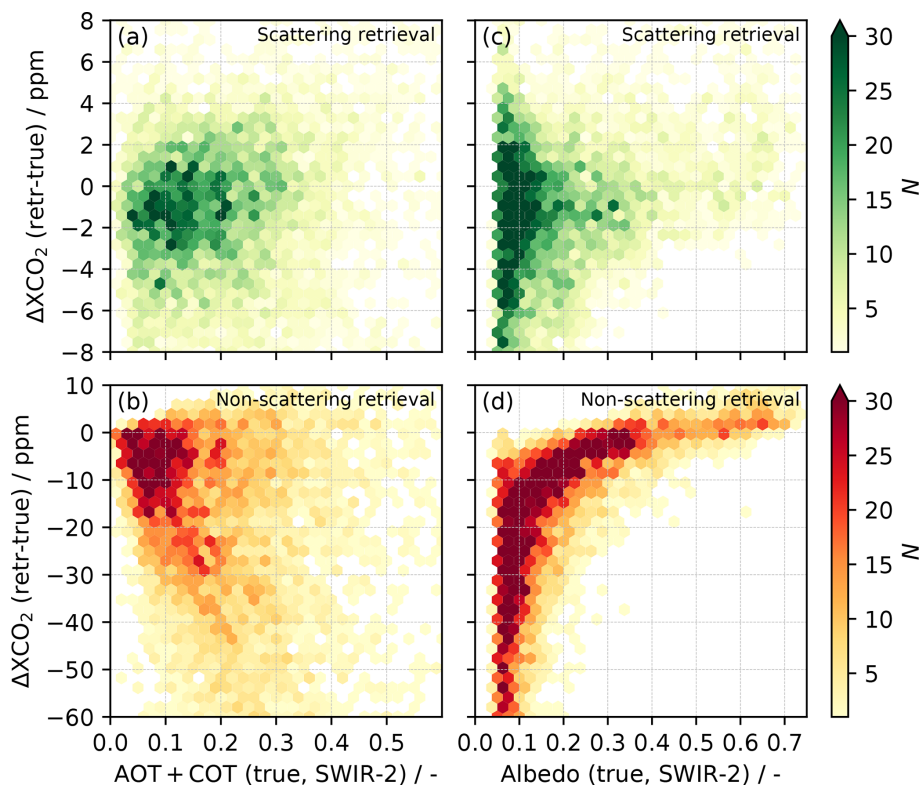


Figure 6. (a, b) XCO₂ retrieval errors as a function of the total particulate optical thickness AOT + COT for scattering (a) and non-scattering (b) RemoTeC retrievals. (c, d) XCO₂ retrieval errors as a function of SWIR-2 surface albedo for scattering (c) and non-scattering (d) RemoTeC retrievals. N denotes the number of retrievals. Note the different ranges of the y axes in the upper and lower panels.

path to some degree as a result of multiple scattering between scattering particles and the surface. Such modifications of the light path will be understood as CO₂ concentrations in the atmosphere that are either too low (overall reduced light path) or too high (overall extended light path) if scattering cannot be accounted for in the retrieval. Which effect dominates is primarily driven by the surface albedo. This is visualized in Fig. 6d that shows the difference between retrieved and true XCO₂ as a function of the surface albedo when scattering by aerosol and cirrus is neglected in the retrieval. Over darker surfaces for which the effect of multiple scattering between aerosol and the surface is limited, aerosol and cirrus particles scattering the incoming solar radiation towards the sensor higher up in the atmosphere become the dominating effect, leading to a reduced light path and underestimation of the XCO₂. Over brighter surfaces for which the effect of multiple scattering becomes dominant, the non-scattering retrieval is more likely to overestimate the CO₂ abundance because the loss of radiation due to an extended light path, resulting from the multiple scattering, is assumed to be caused by more absorbing CO₂ molecules in the atmosphere. Figure 6c shows the difference between retrieved and true XCO₂ as a function of the surface albedo when scattering by aerosol and cirrus is accounted for when retrieving XCO₂ from the syn-

thetic measurements of the proposed satellite concept. It is clear that when aerosol properties are retrieved alongside the CO₂ abundance, the curve-shaped relationship between the XCO₂ error and surface albedo vanishes with no clear error correlation other than XCO₂ errors increasing with decreasing albedo (and thus SNR). Note that errors arising from the Lambertian albedo assumption (BRDF – bidirectional reflectance distribution function – effects) are neglected in the scattering simulations.

Although layers of aerosol and cirrus can be partly accounted for in the retrieval, scenes with thicker clouds and aerosol layers will have to be identified and filtered out in the data processing chain. Such a cloud filter could exploit the different optical depths of the two CO₂ bands in the SWIR-2 window by retrieving XCO₂ from the two CO₂ bands independently (assuming a non-scattering atmosphere) and filtering for discrepancies.

5 Performance evaluation for an urban case study

While the previous section assessed XCO₂ errors for the range of geophysical conditions expected to be encountered on a global scale, this section evaluates the CO₂ monitor-

ing capabilities at an urban scale using high-resolution CO₂ concentration and surface albedo data. Similar to Sect. 4, the high-resolution data are used to simulate synthetic measurements, from which synthetic XCO₂ abundances can be retrieved in order to make a first assessment of the CO₂ monitoring ability of the proposed instrument concept in terms of resolving CO₂ emission plumes.

5.1 Datasets

5.1.1 CO₂ concentration field from the Hestia dataset

To compute a high-resolution three-dimensional field of CO₂ concentrations to be used as input for the radiative transfer simulations, annual estimates of fossil fuel CO₂ emissions for the city of Indianapolis in the year 2015 are used. These data are generated by the Hestia Project (Gurney et al., 2012, 2019) for which the fossil fuel CO₂ emissions are quantified in urban areas down to the scale of individual buildings and streets using a bottom-up approach. The results for the city of Indianapolis are gridded and archived at a spatial resolution of 200 × 200 m². For this study, however, the Hestia Project dataset was gridded to 50 × 50 m² via request to the Hestia research team in order to match the envisaged spatial resolution of the proposed instrument concept. The fossil fuel CO₂ emission rates for Indianapolis at 50 × 50 m² resolution can be seen in Fig. 7a. CO₂ emissions from different sources and sectors like road traffic and point sources (single yellow pixels) can be seen. There is also an apparent emission gradient, with stronger emissions in the city center and weaker emissions towards the suburbs. Hence, the Hestia CO₂ emission data for Indianapolis provide a realistic emission scenario for evaluating the CO₂ monitoring capabilities of the proposed instrument concept. Moreover, the area of the Hestia domain (approx. 34 × 33 km²) is comparable to what the prospective tile size of each observation target area could be.

The Hestia CO₂ emission data are used as input to a Gaussian dispersion model in order to compute a three-dimensional CO₂ concentration field. For a given CO₂ emission rate Q (g s⁻¹), the CO₂ concentration C (g m⁻³) at a given position (x, y, z) downwind of the emitter is calculated as

$$C(x, y, z) = \frac{Q}{2\pi u \sigma_y \sigma_z} \exp\left(\frac{-y^2}{2\sigma_y^2}\right) \left[\exp\left(\frac{-(z-h)^2}{2\sigma_z^2}\right) + \exp\left(\frac{-(z+h)^2}{2\sigma_z^2}\right) \right], \quad (6)$$

where u is the horizontal wind speed in the x direction (along-wind), h is the height of the emitting source (in meters above ground level), and σ_y and σ_z are the standard deviations of the concentration distribution (in meters) in the horizontal across-wind and vertical dimension, respectively; σ_y and σ_z , and hence the spread of the emission plume, depend on the atmospheric instability, i.e., the degree of atmospheric

turbulence and the downwind distance x from the emitting source. Here, we calculate σ_y and σ_z assuming the Pasquill–Gifford stability class C (slightly unstable atmosphere). Furthermore, a constant wind speed $u = 3$ m s⁻² and an emitting source height $h = 75$ m (for all sources) are assumed. This model setup is comparable to similar studies (e.g., Bovensmann et al., 2010; Dennison et al., 2013).

Downwind CO₂ concentrations from each emitting source (pixel) in the Hestia dataset are calculated across an equidistant grid at 50 m resolution in all dimensions, and the contributions from all individual emitting sources (pixels) are subsequently combined to form a three-dimensional CO₂ concentration field over Indianapolis. Figure 7b shows the resulting (vertically integrated) two-dimensional field of (noiseless) XCO₂ enhancements at 50 × 50 m² spatial resolution over a constant background with a surface pressure of 1013 hPa. While weaker diffuse sources like streets cannot be identified, the plumes from stronger point sources are clearly pronounced given the high spatial resolution that allows for a detailed mapping of the plumes. For comparison, Fig. 7c shows the corresponding XCO₂ enhancements assuming a coarser spatial resolution of 2 × 2 km². Although the stronger plumes can still be identified at the coarser resolution, the XCO₂ enhancements are significantly lower and each plume is only sampled by a few pixels. Figure 7d further shows these XCO₂ enhancements in more detail for three along-track excerpts centered at 400, 1500 and 4000 m downwind of the strongest emitter in Indianapolis, with an annual emission rate of 3.24 Mt CO₂ yr⁻¹ in 2015. The positions of the three along-track excerpts are indicated with grey lines in Fig. 7b and c. With a spatial resolution of 2 × 2 km², the along-track plume excerpts are only sampled by one pixel each, with a maximum XCO₂ enhancement of 1.2 ppm. With the envisaged 50 × 50 m² spatial resolution, however, the plume is sampled by 7, 15 and 29 pixels in the along-track dimension 400, 1500 and 4000 m downwind of the emitter, respectively, with maximum XCO₂ enhancements reaching approximately 18, 6 and 3 ppm, respectively. This clearly demonstrates the benefit of an instrument with a high spatial resolution when resolving CO₂ emission plumes from space.

5.1.2 Surface albedo data from Sentinel-2

To accurately simulate the instrument SNR and hence the measurement noise, it is important to know how large a fraction of the solar radiation incident on the Earth's surface is reflected back towards space. To get realistic estimates of the surface albedo within the Hestia Indianapolis domain, data from the European Sentinel-2 satellites are used. The multispectral instrument aboard Sentinel-2 measures the TOA radiance in 13 spectral bands with a spatial resolution ranging from 10 × 10 m² to 60 × 60 m². For this study, we use the Sentinel-2 L1C radiances measured in spectral band 12 (centered at approx. 2200 nm) at a spatial resolution of 20 × 20 m². The software Sen2Cor (ESA, 2018) is employed

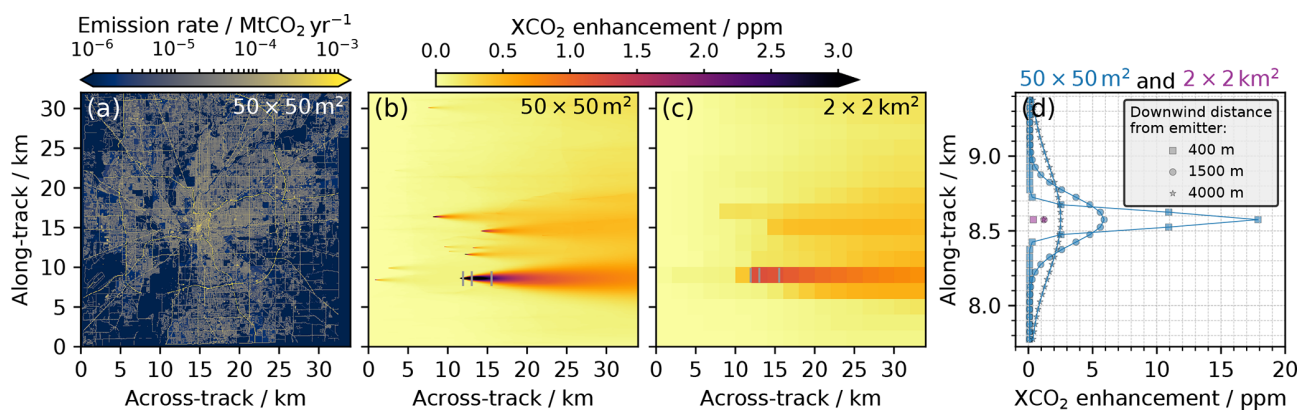


Figure 7. (a) Hestia fossil fuel CO₂ emission data for Indianapolis in 2015 at 50 × 50 m² spatial resolution. (b) Corresponding field of vertically integrated XCO₂ enhancements at 50 × 50 m² spatial resolution with respect to a constant background, computed using the Hestia CO₂ emission data and a Gaussian dispersion model. Panel (c) is the same as (b), but at 2 × 2 km² spatial resolution. (d) Per-pixel XCO₂ enhancements for three along-track excerpts centered at 400, 1500 and 4000 m downwind of the emitter at 50 × 50 m² and 2 × 2 km² spatial resolution. The respective positions of the along-track excerpts are indicated by the small grey lines in (b) and (c). The x and y dimensions of the Hestia Indianapolis domain are illustrated as hypothetical satellite across-track and along-track dimensions, respectively.

to compute the corresponding L2 surface reflectances from the L1C TOA radiances through a so-called atmospheric correction.

Surface reflectance data for the month of July 2018 are computed and re-gridded (using nearest neighbor) to the envisaged spatial resolution of 50 × 50 m². The surface reflectance for Sentinel-2 pixels classified as vegetation is scaled by a factor of 0.82 in order to account for the generally lower reflectance by vegetation in the SWIR-2 window compared to Sentinel-2's band 12. The scaling factor has been derived using spectral reflectance data from the ECOSTRESS spectral library (Baldrige et al., 2009; Meerdink et al., 2019). Figure 8b shows the gridded surface reflectance data for Indianapolis together with a corresponding red–green–blue (RGB) composite (Fig. 8a) using Sentinel-2 data from the bands centered at red, green and blue wavelengths as a reference. The scaled and gridded Sentinel-2 surface reflectance data are taken as representative for a constant Lambertian surface albedo within the entire SWIR-2 window. Figure S1 in the Supplement shows spectral reflectances in the SWIR spectral region for various urban materials using data from the Spectral Library of Imperious Urban Materials (SLUM; Kotthaus et al., 2014). The small spectral variations within the SWIR-2 spectral window used in this study indicate that the true spectral signatures of the surface albedo could be fitted with sufficient precision using the second-order polynomial during the retrieval, and hence the assumption of a constant albedo is reasonable for this study.

The average surface reflectance within the Hestia domain is 0.13. Despite annual variability in surface reflectance, mainly due to changes in vegetation and/or crops, this is a value representative throughout most of the year. For comparison, average surface reflectances from the same

source for January (snow-free days), April and October 2018 amount to 0.11, 0.17 and 0.11, respectively.

5.1.3 Background data from CarbonTracker

Background data, including vertical profiles of CO₂, H₂O, temperature and pressure, are taken for 15 July 2016 from the CarbonTracker CT2017 dataset (Peters et al., 2007, with updates documented at <http://carbontracker.noaa.gov>, last access: 18 March 2019). The CarbonTracker CT2017 data over Indianapolis are provided at a spatial resolution of 1° × 1°, meaning that the entire Hestia Indianapolis domain is covered by one single CarbonTracker pixel, leading to a constant background data field.

5.2 Simulated CO₂ plume observations

As in Sect. 4, the above sets of input data are used to simulate synthetic measurements (spectral radiances) and the corresponding instrument noise of the proposed instrument concept using the forward model and the instrument noise model (Sect. 3). The SZA is calculated for the given coordinates in the Hestia domain assuming the sun-synchronous orbit described in Sect. 2 and an observation date of 15 July 2018, which translates to an SZA of about 18°. Corresponding XCO₂ abundances are then retrieved from the simulated spectral radiances such that the ability to observe the CO₂ emission plumes from the Hestia Indianapolis data can be evaluated. In this first assessment we focus solely on the instrument performance in terms of its CO₂ plume quantification capabilities, and hence we perform the high-resolution simulations with the expected instrument-noise-induced errors only, i.e., by assuming a non-scattering atmosphere.

Figure 9a shows the retrieved field of XCO₂ enhancements with respect to the retrieved background XCO₂ over

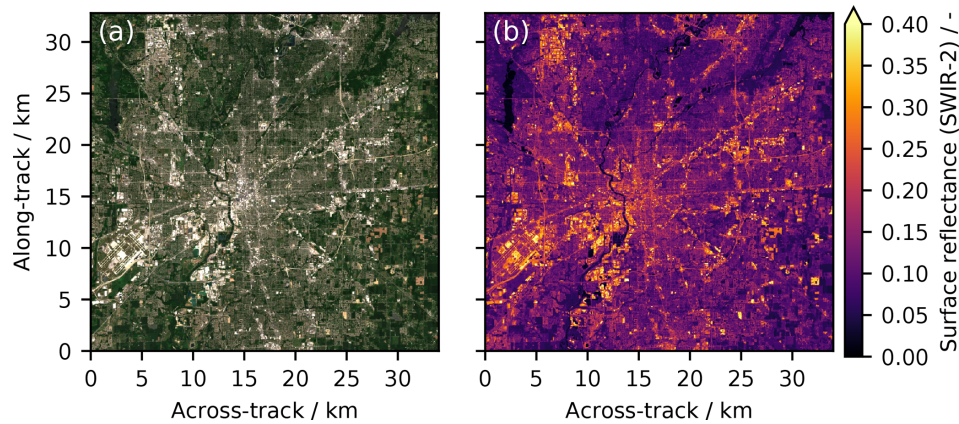


Figure 8. (a) Sentinel-2 true-color RGB image of Indianapolis (Hestia domain) at $50 \times 50 \text{ m}^2$ spatial resolution derived from Sentinel-2 measurements in July 2018. (b) Corresponding surface reflectance data using data from Sentinel-2's spectral band 12 centered at approximately 2200 nm, scaled to the SWIR-2 spectral window. Again, the x and y dimensions of the Hestia Indianapolis domain are illustrated as hypothetical satellite across-track and along-track dimensions, respectively.

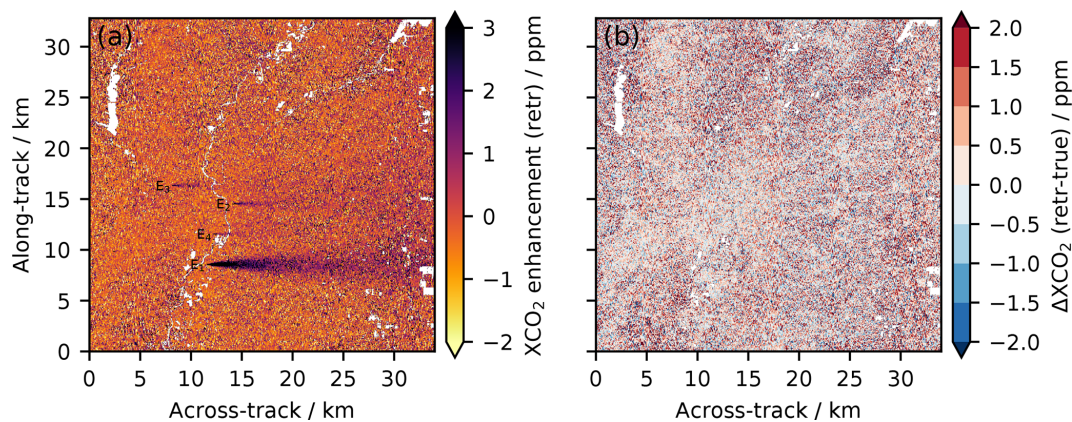


Figure 9. (a) XCO₂ enhancements with respect to the background retrieved from the simulated synthetic measurements over the Hestia Indianapolis domain under non-scattering conditions. Locations of the four strongest point sources are labeled with E_{1-4} . (b) Corresponding deviations between retrieved ("retr") and true XCO₂. Dark scenes with albedo < 0.05 have been filtered out due to unreliable XCO₂ retrievals.

the Hestia domain. The CO₂ plume from the strongest point source, E_1 , with an annual CO₂ emission rate of $Q_1 = 3.24 \text{ MtCO}_2 \text{ yr}^{-1}$, is clearly resolved with local XCO₂ enhancements well above 100 ppm close to the emitting source. Although they emit considerably less CO₂, the plumes from the second- and third-strongest point sources, E_2 and E_3 , with annual CO₂ emission rates of $Q_2 = 0.55 \text{ MtCO}_2 \text{ yr}^{-1}$ and $Q_3 = 0.48 \text{ MtCO}_2 \text{ yr}^{-1}$, respectively, can be clearly separated from the background as well. The plume from the fourth-strongest point source, E_4 , with an annual CO₂ emission rate of $Q_4 = 0.32 \text{ MtCO}_2 \text{ yr}^{-1}$, can also be observed but is partly obscured by filtered-out dark surface areas for which retrieval errors are too high. Plumes from weaker point sources ($\lesssim 0.1 \text{ MtCO}_2 \text{ yr}^{-1}$) and other sources like streets and highways cannot be identified given the spatial resolution and instrument noise errors of the proposed instrument.

One concern with high-resolution CO₂ remote sensing is the impact of albedo heterogeneity at an urban scale at such a high spatial resolution. For the non-scattering scenario simulated here, the albedo fitted by the retrieval algorithm matches the reference input albedo with an average (absolute) deviation of 0.14 %, and there is consequently no spatial variability in the accuracy of the albedo retrieval that in turn affects the XCO₂ retrieval accuracy. There is, however, the evident effect that a higher albedo leads to a higher SNR and hence a generally lower noise error. This is evident from Fig. 9b, showing the difference between the retrieved and true XCO₂, thus illustrating an instantaneous noise error field that would be expected for a single satellite overpass. Generally, the deviations from the true XCO₂ are smaller over areas of brighter surfaces like concrete, whereas the deviations are larger over dark surfaces like forests (see also Fig. 8). The effect of albedo heterogeneity in combination with scattering

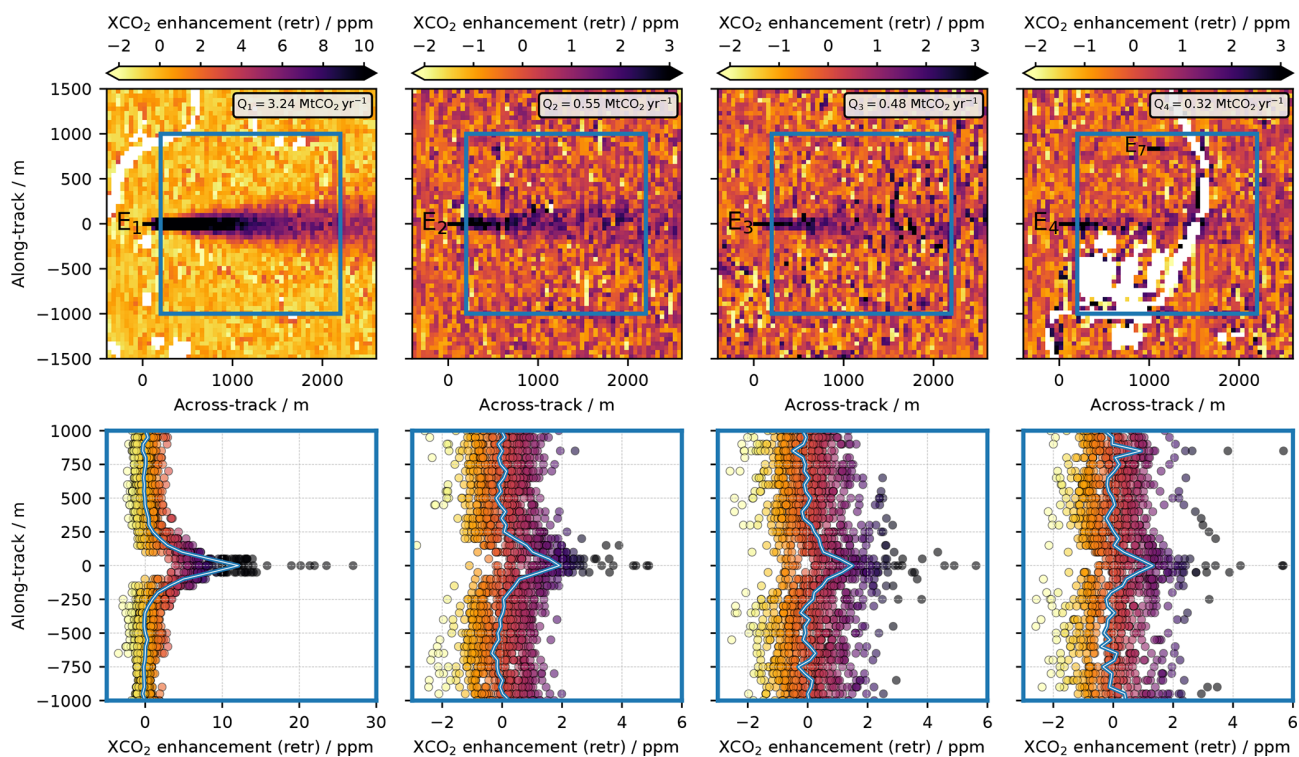


Figure 10. Upper panels: retrieved two-dimensional fields of XCO₂ enhancements in the vicinity of the four strongest CO₂ emitters E_1 , E_2 , E_3 and E_4 within the Hestia Indianapolis dataset. Lower panels: corresponding per-pixel (circles) and average (solid lines) along-track XCO₂ enhancements within the area 200 to 2200 m downwind and -1000 to 1000 across-wind of the respective emitters. The blue rectangles in the upper panels show the areas from which the corresponding per-pixel and average along-track XCO₂ enhancements, depicted in the respective lower panels, are extracted and calculated. The color of the circles follows the color bars in the respective upper panels.

particles is not addressed in this paper and will have to be analyzed in future studies.

Across the entire Hestia domain (but excluding dark scenes with albedo < 0.05) 68 % and 95 % of the XCO₂ retrievals deviate from the true XCO₂ by less than 1.1 and 2.3 ppm, respectively. This is comparable to the noise error obtained for the global trial ensemble in Sect. 4.1 (1.1 and 2.0 ppm, respectively).

Figure 10 shows close-ups of the simulated XCO₂ enhancement field (upper panels) in the vicinity of the four strongest emitters in the Hestia Indianapolis dataset (E_1 – E_4 in Fig. 9a), along with the corresponding per-pixel and average along-track XCO₂ enhancements (lower panels) for the range 200–2200 m downwind of the respective emitting sources. Enhancements from the 200 m closest to each emitting source are excluded as those scenes could likely be obscured by condensate in a real situation.

The plume of the strongest emitter E_1 in Indianapolis with an annual emission rate of $Q_1 = 3.24 \text{ MtCO}_2 \text{ yr}^{-1}$ is clearly resolved. Within the area 200–2200 m downwind of the emitting source (blue square), maximum enhancements exceed 25 ppm, and in total, approximately 200 (60) pixels have enhancements above 4 ppm (8 ppm), representing enhancements of approximately 1 % (2 %) with respect to the

background. The average along-track XCO₂ enhancement 200–2200 m downwind of the emitting source (blue and white line) reaches 12 ppm. The plumes from the second- and third-strongest emitters, E_2 and E_3 , which are approximately 6 times weaker than E_1 with annual emission rates of $Q_2 = 0.55$ and $Q_3 = 0.48 \text{ MtCO}_2 \text{ yr}^{-1}$, respectively, have considerably lower XCO₂ enhancements but can nevertheless clearly be separated from the background with distinct increments in both per-pixel and average XCO₂ enhancements within the area 200–2200 m downwind of the emitters (blue squares). While the background fields vary from approximately -1 to 1 ppm due to instrument noise, the per-pixel plume enhancements vary from approximately 0.5 to 3 ppm, with single enhancements exceeding 4 ppm close to the emitting source. The average along-track XCO₂ enhancements 200–2200 m downwind of the emitting sources (blue and white lines) reach 1.9 and 1.5 ppm for E_2 and E_3 , respectively. Despite being partly obscured by filtered-out dark surfaces (water), the plume from the fourth-strongest emitter E_4 , with an annual emission rate of $Q_4 = 0.32 \text{ MtCO}_2 \text{ yr}^{-1}$, can also be separated from the background both when looking at the two-dimensional field and the per-pixel enhancements within the area 200–2200 m downwind of the emitter. With maximum average XCO₂ enhancements of at most

approximately 1.3 ppm, the proposed instrument concept is, however, approaching the limit of what it could achieve in terms of CO₂ plume observations under favorable conditions, i.e., when the effect of aerosol-induced errors is neglected and the SZA is relatively low. A second peak in the average along-track XCO₂ enhancements is observed approximately 850 m above (north of) the fourth-strongest emitter E_4 . This enhancement stems from the CO₂ plume from the seventh-strongest emitter in Indianapolis (labeled E_7 in the top right panel of Fig. 10), with an annual emission rate of $Q_7 = 0.1 \text{ MtCO}_2 \text{ yr}^{-1}$. Quantifying the CO₂ emission rate from such a weak source is, however, not realistic given the low sampling density (especially further downwind) in combination with the weak per-pixel enhancements.

6 Conclusions

To follow the progress on reducing anthropogenic CO₂ emissions worldwide, independent monitoring systems are of key importance. In this paper, we present the concept of a compact spaceborne imaging spectrometer with a high spatial resolution of $50 \times 50 \text{ m}^2$ targeting the monitoring of localized CO₂ emissions. We further demonstrate how the instrument concept could resolve CO₂ emission plumes from localized point sources like medium-sized power plants, thus having the potential to contribute to the independent large-scale verification of reported CO₂ emissions at the facility level.

Through radiative transfer simulations using a global trial ensemble, a preliminary yet realistic instrument design and an instrument noise model, we show that the expected instrument-noise-induced XCO₂ errors are smaller than 1.1 and 2.0 ppm for 68 % and 95 % of the retrievals, respectively, using the SWIR-2 spectral setup covering the CO₂ absorption bands near 2000 nm. For the SWIR-1 spectral setup covering the weaker CO₂ absorption bands near 1600 nm, the instrument-noise-induced XCO₂ errors are significantly higher, making it inadequate for the proposed instrument concept. Although the main focus in this paper is on the performance of the proposed CO₂ monitoring instrument concept, we could also show that despite the usage of a single spectral window and a relatively coarse spectral resolution of 1.29 nm, scattering by highly complex atmospheric aerosol compositions can be partly accounted for during XCO₂ retrievals on the global scale, limiting the deviation from the true XCO₂ to at most 4.0 ppm for two-thirds of the retrievals. This gives us confidence that accurate two-dimensional fields of XCO₂ enhancements could be retrieved from real spectra measured by the proposed instrument concept. A reasonable a priori state vector with respect to the aerosol properties (e.g., provided through models or a companion aerosol instrument; Hasekamp et al., 2019) would, however, still be important. As an example, a multi-angle polarimeter instrument is planned to fly together with the CO₂ instrument on-

board the CO2M mission in order to minimize systematic XCO₂ errors (ESA, 2019).

Using high-resolution CO₂ emission data for the city of Indianapolis together with a Gaussian dispersion model, corresponding high-resolution albedo data and additional radiative transfer simulations, we have clearly demonstrated that the instrument is well suited for the task of the spaceborne CO₂ monitoring of large and medium-sized power plants and can (only limited by its own instrument noise) resolve emission plumes from point sources with an emission source strength down to the order of $0.3 \text{ MtCO}_2 \text{ yr}^{-1}$. This is well below the target emission source strength of $1 \text{ MtCO}_2 \text{ yr}^{-1}$, hence leaving a significant margin for additional error sources and aspects not yet addressed here.

Given the results from this first performance assessment, the proposed instrument concept demonstrates clear potential for the independent quantification of CO₂ emissions from medium-sized power plants ($1\text{--}10 \text{ MtCO}_2 \text{ yr}^{-1}$), which are currently not targeted by other planned spaceborne CO₂ monitoring missions. On the local scale (Indianapolis), we have constrained the present analysis to a day in July using a rather simplistic Gaussian dispersion model that assumes constant atmospheric stability and (unidirectional) horizontal wind speed. It might be that the ability to resolve CO₂ emission plumes will become more, perhaps even too, challenging under certain more realistic conditions. Nevertheless, these first results are certainly promising and encourage further studies.

The high spatial resolution needed to resolve emission plumes from localized sources like medium-sized power plant does, however, imply limitations in terms of spatial coverage arising from the narrow swath (50 km assuming 1000 detector pixels in the spatial dimension) and the forward motion compensation. Hence, a single satellite with the proposed instrument concept could not quantify CO₂ emissions at the local to regional scale with dense global coverage and high temporal resolution but would have to be restricted to some predefined targets. The relatively compact design with a single spectral window could, however, allow for the deployment of a fleet of instruments and hence the independent monitoring of localized CO₂ emissions on a larger scale with high temporal resolution. As an alternative to a fleet of satellites, the proposed instrument concept could also prove useful in synergy with a spaceborne CO₂ lidar (e.g., Kiemle et al., 2017); the passive spectrometer would benefit from the lidar's accuracy and knowledge of the light path, and the lidar would benefit from the spectrometer's imaging capability.

With the successful demonstration in this paper, i.e., that CO₂ emission plumes from medium-sized power plants can be resolved from space with a compact yet realistic instrument design, the next step will be to analyze the ability to quantify the corresponding CO₂ emission rates from the two-dimensional fields of synthetically retrieved XCO₂ enhancements. This follow-up study will be conducted for different seasons (with varying surface albedo

and solar zenith angles), meteorological conditions and emission source strengths using large eddy, rather than Gaussian, modeling of the CO₂ plume dispersion. Although the effect of aerosols has partly been assessed on the global scale in this study, information on the properties and distribution of aerosols should also be included in the local-scale simulations in order to better understand the instrument's ability to resolve and quantify localized CO₂ emissions under more realistic conditions. Such an in-depth aerosol analysis is, however, the task of further future studies.

Data availability. Hestia Project data at 50 × 50 m² spatial resolution are available from KG upon request (Hestia Project data at original 200 × 200 m² spatial resolution are available at <https://doi.org/10.18434/T4/1503341>; Gurney et al., 2018). Sentinel-2 data are available at <https://scihub.copernicus.eu/dhus/#/home> (last access: 9 July 2019). ECOSTRESS Spectral Library data are available at <https://speclib.jpl.nasa.gov> (last access: 12 February 2019). CarbonTracker CT2017 data are available at <http://carbontracker.noaa.gov> (last access: 18 March 2019). SLUM data are available at <http://www.met.reading.ac.uk/micromet/LUMA/SLUM.html> (last access: 18 March 2020).

Supplement. The supplement related to this article is available online at: <https://doi.org/10.5194/amt-13-2887-2020-supplement>.

Author contributions. JS developed the instrument noise model, performed the simulations and wrote most of the paper. DK led the instrument design work. JW performed the spectral sizing. CP assisted in developing the instrument noise model and performed the FMC analysis. IS did the optical design. KRG and JL developed and provided the Hestia Project CO₂ emission data. JS, DK, JW, CP, IS, AR and AB defined the mission concept and instrument design. AR and AB led the study.

Competing interests. The authors declare that they have no conflict of interest.

Acknowledgements. We kindly acknowledge all persons and institutions that made their data available to us for this study. CARMA v3.0 CO₂ emission data for power plants worldwide were provided by Kevin Ummel. Sentinel-2 data used to derive high-resolution surface reflectance data were provided by the ESA through the Copernicus Open Access Hub. Spectral reflectance data used to scale the Sentinel-2 surface reflectance data were reproduced from the ECOSTRESS Spectral Library through the courtesy of the Jet Propulsion Laboratory, California Institute of Technology, Pasadena, California, USA. CarbonTracker CT2017 data were provided by NOAA ESRL, Boulder, Colorado, USA. Spectral reflectance data for urban materials (see the Supplement) were reproduced from the Spectral Library of Impervious Urban Materials (SLUM) through the courtesy of the University of Reading, UK. We also thank Peter Haschberger, Claas Köhler, Günter Lichten-

berg, Andreas Baumgartner, Christoph Kiemle, Luca Bugliaro, Julian Kostinek and Andreas Luther for valuable input on the mission concept, instrument design and/or a previous version of this paper.

Financial support. The article processing charges for this open-access publication were covered by a Research Centre of the Helmholtz Association.

Review statement. This paper was edited by Andreas Richter and reviewed by Luis Guanter and one anonymous referee.

References

- Abdollahi, A., Dastranj, M., and Riahi, A.: Satellite Attitude Tracking for Earth Pushbroom Imaginary with Forward Motion Compensation, *International Journal of Control and Automation*, 7, 437–446, <https://doi.org/10.14257/ijca.2014.7.1.39>, 2014.
- Baldrige, A., Hook, S., Grove, C., and Rivera, G.: The ASTER spectral library version 2.0, *Remote Sens. Environ.*, 113, 711–715, <https://doi.org/10.1016/j.rse.2008.11.007>, 2009.
- Bovensmann, H., Buchwitz, M., Burrows, J. P., Reuter, M., Krings, T., Gerilowski, K., Schneising, O., Heymann, J., Tretner, A., and Erzinger, J.: A remote sensing technique for global monitoring of power plant CO₂ emissions from space and related applications, *Atmos. Meas. Tech.*, 3, 781–811, <https://doi.org/10.5194/amt-3-781-2010>, 2010.
- Buchwitz, M., Reuter, M., Bovensmann, H., Pillai, D., Heymann, J., Schneising, O., Rozanov, V., Krings, T., Burrows, J. P., Boesch, H., Gerbig, C., Meijer, Y., and Löscher, A.: Carbon Monitoring Satellite (CarbonSat): assessment of atmospheric CO₂ and CH₄ retrieval errors by error parameterization, *Atmos. Meas. Tech.*, 6, 3477–3500, <https://doi.org/10.5194/amt-6-3477-2013>, 2013.
- Buil, C., Pascal, V., Loesel, J., Pierangelo, C., Roucayrol, L., and Tauziède, L.: A new space instrumental concept for the measurement of CO₂ concentration in the atmosphere, in: *SPIE 8176, Sensors, Systems, and Next-Generation Satellites XV*, SPIE, 8176, 535–545, <https://doi.org/10.1117/12.897598>, 2011.
- Butz, A., Hasekamp, O. P., Frankenberg, C., and Aben, I.: Retrievals of atmospheric CO₂ from simulated space-borne measurements of backscattered near-infrared sunlight: accounting for aerosol effects, *Appl. Optics*, 48, 3322–3336, <https://doi.org/10.1364/AO.48.003322>, 2009.
- Butz, A., Hasekamp, O., Frankenberg, C., Vidot, J., and Aben, I.: CH₄ retrievals from space-based solar backscatter measurements: Performance evaluation against simulated aerosol and cirrus loaded scenes, *J. Geophys. Res.-Atmos.*, 115, D24, <https://doi.org/10.1029/2010JD014514>, 2010.
- Butz, A., Guerlet, S., Hasekamp, O., Schepers, D., Galli, A., Aben, I., Frankenberg, C., Hartmann, J.-M., Tran, H., Kuze, A., Keppel-Aleks, G., Toon, G., Wunch, D., Wennberg, P., Deutscher, N., Griffith, D., Macatangay, R., Messerschmidt, J., Notholt, J., and Warneke, T.: Toward accurate CO₂ and CH₄ observations from GOSAT, *Geophys. Res. Lett.*, 38, 14, <https://doi.org/10.1029/2011GL047888>, 2011.
- Butz, A., Galli, A., Hasekamp, O., Landgraf, J., Tol, P., and Aben, I.: TROPOMI aboard Sentinel-5 Precursor: Prospec-

- tive performance of CH₄ retrievals for aerosol and cirrus loaded atmospheres, *Remote Sens. Environ.*, 120, 267–276, <https://doi.org/10.1016/j.rse.2011.05.030>, 2012.
- Butz, A., Orphal, J., Checa-Garcia, R., Friedl-Vallon, F., von Clarmann, T., Bovensmann, H., Hasekamp, O., Landgraf, J., Knigge, T., Weise, D., Sqalli-Houssini, O., and Kemper, D.: Geostationary Emission Explorer for Europe (G3E): mission concept and initial performance assessment, *Atmos. Meas. Tech.*, 8, 4719–4734, <https://doi.org/10.5194/amt-8-4719-2015>, 2015.
- Chatterjee, A., Gierach, M. M., Sutton, A. J., Feely, R. A., Crisp, D., Eldering, A., Gunson, M. R., O'Dell, C. W., Stephens, B. B., and Schimel, D. S.: Influence of El Niño on atmospheric CO₂ over the tropical Pacific Ocean: Findings from NASA's OCO-2 mission, *Science*, 358, 6360, <https://doi.org/10.1126/science.aam5776>, 2017.
- Crisp, D., Atlas, R., Breon, F.-M., Brown, L., Burrows, J., Ciais, P., Connor, B., Doney, S., Fung, I., Jacob, D., Miller, C., O'Brien, D., Pawson, S., Randerson, J., Rayner, P., Salawitch, R., Sander, S., Sen, B., Stephens, G., Tans, P., Toon, G., Wennberg, P., Wofsy, S., Yung, Y., Kuang, Z., Chudasama, B., Sprague, G., Weiss, B., Pollock, R., Kenyon, D., and Schroll, S.: The Orbiting Carbon Observatory (OCO) mission, *Adv. Space Res.*, 34, 700–709, <https://doi.org/10.1016/j.asr.2003.08.062>, 2004.
- Crisp, D., Pollock, H. R., Rosenberg, R., Chapsky, L., Lee, R. A. M., Oyafuso, F. A., Frankenberg, C., O'Dell, C. W., Bruegge, C. J., Doran, G. B., Eldering, A., Fisher, B. M., Fu, D., Gunson, M. R., Mandrake, L., Osterman, G. B., Schwandner, F. M., Sun, K., Taylor, T. E., Wennberg, P. O., and Wunch, D.: The on-orbit performance of the Orbiting Carbon Observatory-2 (OCO-2) instrument and its radiometrically calibrated products, *Atmos. Meas. Tech.*, 10, 59–81, <https://doi.org/10.5194/amt-10-59-2017>, 2017.
- Dennison, P. E., Thorpe, A. K., Pardyjak, E. R., Roberts, D. A., Qi, Y., Green, R. O., Bradley, E. S., and Funk, C. C.: High spatial resolution mapping of elevated atmospheric carbon dioxide using airborne imaging spectroscopy: Radiative transfer modeling and power plant plume detection, *Remote Sens. Environ.*, 139, 116–129, <https://doi.org/10.1016/j.rse.2013.08.001>, 2013.
- Eldering, A., Wennberg, P. O., Crisp, D., Schimel, D. S., Gunson, M. R., Chatterjee, A., Liu, J., Schwandner, F. M., Sun, Y., O'Dell, C. W., Frankenberg, C., Taylor, T., Fisher, B., Osterman, G. B., Wunch, D., Hakkarainen, J., Tamminen, J., and Weir, B.: The Orbiting Carbon Observatory-2 early science investigations of regional carbon dioxide fluxes, *Science*, 358, 6360, <https://doi.org/10.1126/science.aam5745>, 2017.
- Eldering, A., Taylor, T. E., O'Dell, C. W., and Pavlick, R.: The OCO-3 mission: measurement objectives and expected performance based on 1 year of simulated data, *Atmos. Meas. Tech.*, 12, 2341–2370, <https://doi.org/10.5194/amt-12-2341-2019>, 2019.
- ESA: Sen2Cor Configuration and User Manual, available at: http://step.esa.int/thirdparties/sen2cor/2.5.5/docs/S2-PDGS-MPC-L2A-SUM-V2.5.5_V2.pdf (last access: 2 June 2020), S2-PDGS-MPC-L2A-SUM-V2.5.5, 2018.
- ESA: Copernicus CO₂ Monitoring Mission Requirements Document, available at: https://esamultimedia.esa.int/docs/EarthObservation/CO2M_MRD_v2.0_Issued20190927.pdf (last access: 12 November 2019), EOP-SM/3088/YM-ym, 2019.
- Guerlet, S., Basu, S., Butz, A., Krol, M., Hahne, P., Houweling, S., Hasekamp, O. P., and Aben, I.: Reduced carbon uptake during the 2010 Northern Hemisphere summer from GOSAT, *Geophys. Res. Lett.*, 40, 2378–2383, <https://doi.org/10.1002/grl.50402>, 2013.
- Gurney, K. R., Razlivanov, I., Song, Y., Zhou, Y., Benes, B., and Abdul-Massih, M.: Quantification of Fossil Fuel CO₂ Emissions on the Building/Street Scale for a Large U.S. City, *Environ. Sci. Technol.*, 46, 12194–12202, <https://doi.org/10.1021/es3011282>, 2012.
- Gurney, K. R., Patarasuk, R., Liang, J., Zhou, Y., O'Keefe, D., Hutchins, M., Huang, J., Song, Y., Rao, P., Wong, T. M., and Whetstone, J. R.: Hestia Fossil Fuel Carbon Dioxide Emissions for Indianapolis, Indiana, NIST, <https://doi.org/10.18434/T4/1503341>, 2018.
- Gurney, K. R., Liang, J., O'Keefe, D., Patarasuk, R., Hutchins, M., Huang, J., Rao, P., and Song, Y.: Comparison of Global Downscaled Versus Bottom-Up Fossil Fuel CO₂ Emissions at the Urban Scale in Four U.S. Urban Areas, *J. Geophys. Res.-Atmos.*, 124, 2823–2840, <https://doi.org/10.1029/2018JD028859>, 2019.
- Hakkarainen, J., Jalongo, I., and Tamminen, J.: Direct space-based observations of anthropogenic CO₂ emission areas from OCO-2, *Geophys. Res. Lett.*, 43, 11400–11406, <https://doi.org/10.1002/2016GL070885>, 2016.
- Hasekamp, O. P., Fu, G., Rusli, S. P., Wu, L., Di Noia, A., van de Brugh, J., Landgraf, J., Smit, J. M., Rietjens, J., and van Amerongen, A.: Aerosol measurements by SPEXone on the NASA ACE mission: expected retrieval capabilities, *J. Quant. Spectrosc. Ra.*, 227, 170–184, <https://doi.org/10.1016/j.jqsrt.2019.02.006>, 2019.
- Hess, M. and Wiegner, M.: COP: a data library of optical properties of hexagonal ice crystals, *Appl. Optics*, 33, 7740–7746, <https://doi.org/10.1364/AO.33.007740>, 1994.
- Hess, M., Koelemeijer, R. B., and Stammes, P.: Scattering matrices of imperfect hexagonal ice crystals, *J. Quant. Spectrosc. Ra.*, 60, 301–308, [https://doi.org/10.1016/S0022-4073\(98\)00007-7](https://doi.org/10.1016/S0022-4073(98)00007-7), 1998.
- IEA: Global Energy and CO₂ Status Report 2018: The latest trends in energy and emissions in 2018, available at: https://webstore.iea.org/download/direct/2461?filename=global_energy_and_co2_status_report_2018.pdf, last access: 18 November 2019.
- Jongaramrungruang, S., Frankenberg, C., Matheou, G., Thorpe, A. K., Thompson, D. R., Kuai, L., and Duren, R. M.: Towards accurate methane point-source quantification from high-resolution 2-D plume imagery, *Atmos. Meas. Tech.*, 12, 6667–6681, <https://doi.org/10.5194/amt-12-6667-2019>, 2019.
- Kiemle, C., Ehret, G., Amediek, A., Fix, A., Quatrevalet, M., and Wirth, M.: Potential of Spaceborne Lidar Measurements of Carbon Dioxide and Methane Emissions from Strong Point Sources, *Remote Sens.*, 9, 11, <https://doi.org/10.3390/rs9111137>, 2017.
- Kort, E. A., Frankenberg, C., Miller, C. E., and Oda, T.: Space-based observations of megacity carbon dioxide, *Geophys. Res. Lett.*, 39, 17, <https://doi.org/10.1029/2012GL052738>, 2012.
- Kotthaus, S., Smith, T. E., Wooster, M. J., and Grimmond, C.: Derivation of an urban materials spectral library through emittance and reflectance spectroscopy, *ISPRS J. Photogramm.*, 94, 194–212, <https://doi.org/10.1016/j.isprsjprs.2014.05.005>, 2014.
- Kuhlmann, G., Broquet, G., Marshall, J., Clément, V., Löscher, A., Meijer, Y., and Brunner, D.: Detectability of CO₂ emission plumes of cities and power plants with the Coperni-

- cus Anthropogenic CO₂ Monitoring (CO2M) mission, *Atmos. Meas. Tech.*, 12, 6695–6719, <https://doi.org/10.5194/amt-12-6695-2019>, 2019.
- Kuze, A., Suto, H., Nakajima, M., and Hamazaki, T.: Thermal and near infrared sensor for carbon observation Fourier-transform spectrometer on the Greenhouse Gases Observing Satellite for greenhouse gases monitoring, *Appl. Optics*, 48, 6716–6733, <https://doi.org/10.1364/AO.48.006716>, 2009.
- Kuze, A., Suto, H., Shiomi, K., Kawakami, S., Tanaka, M., Ueda, Y., Deguchi, A., Yoshida, J., Yamamoto, Y., Kataoka, F., Taylor, T. E., and Buijs, H. L.: Update on GOSAT TANSO-FTS performance, operations, and data products after more than 6 years in space, *Atmos. Meas. Tech.*, 9, 2445–2461, <https://doi.org/10.5194/amt-9-2445-2016>, 2016.
- Liu, J., Bowman, K. W., Schimel, D. S., Parazoo, N. C., Jiang, Z., Lee, M., Bloom, A. A., Wunch, D., Frankenberg, C., Sun, Y., O'Dell, C. W., Gurney, K. R., Menemenlis, D., Gierach, M., Crisp, D., and Eldering, A.: Contrasting carbon cycle responses of the tropical continents to the 2015–2016 El Niño, *Science*, 358, 6360, <https://doi.org/10.1126/science.aam5690>, 2017.
- Liu, Y., Wang, J., Yao, L., Chen, X., Cai, Z., Yang, D., Yin, Z., Gu, S., Tian, L., Lu, N., and Lyu, D.: The TanSat mission: preliminary global observations, *Sci. Bull.*, 63, 1200–1207, <https://doi.org/10.1016/j.scib.2018.08.004>, 2018.
- Maksyutov, S., Takagi, H., Valsala, V. K., Saito, M., Oda, T., Saeki, T., Belikov, D. A., Saito, R., Ito, A., Yoshida, Y., Morino, I., Uchino, O., Andres, R. J., and Yokota, T.: Regional CO₂ flux estimates for 2009–2010 based on GOSAT and ground-based CO₂ observations, *Atmos. Chem. Phys.*, 13, 9351–9373, <https://doi.org/10.5194/acp-13-9351-2013>, 2013.
- Meerdink, S., Hook, S., Abbott, E., and Roberts, D.: The ECOSTRESS spectral library version 1.0, *Remote Sens. Environ.*, 230, 111196, <https://doi.org/10.1016/j.rse.2019.05.015>, 2019.
- Meirink, J. F., Eskes, H. J., and Goede, A. P. H.: Sensitivity analysis of methane emissions derived from SCIAMACHY observations through inverse modelling, *Atmos. Chem. Phys.*, 6, 1275–1292, <https://doi.org/10.5194/acp-6-1275-2006>, 2006.
- Moore III, B., Crowell, S. M. R., Rayner, P. J., Kumer, J., O'Dell, C. W., O'Brien, D., Utembe, S., Polonsky, I., Schimel, D., and Lemen, J.: The Potential of the Geostationary Carbon Cycle Observatory (GeoCarb) to Provide Multi-scale Constraints on the Carbon Cycle in the Americas, *Front. Environ. Sci.*, 6, 109, <https://doi.org/10.3389/fenvs.2018.00109>, 2018.
- Nakajima, M., Kuze, A., and Suto, H.: The current status of GOSAT and the concept of GOSAT-2, in: *SPIE 8533, Sensors, Systems, and Next-Generation Satellites XVI*, SPIE, 8533, 21–30, <https://doi.org/10.1117/12.974954>, 2012.
- Nassar, R., Hill, T. G., McLinden, C. A., Wunch, D., Jones, D. B. A., and Crisp, D.: Quantifying CO₂ Emissions From Individual Power Plants From Space, *Geophys. Res. Lett.*, 44, 10045–10053, <https://doi.org/10.1002/2017GL074702>, 2017.
- NOAA: Global carbon dioxide growth in 2018 reached 4th highest on record, available at: <https://www.noaa.gov/news/global-carbon-dioxide-growth-in-2018-reached-4th-highest-on-record>, last access: 14 May 2019.
- Parazoo, N. C., Bowman, K., Frankenberg, C., Lee, J.-E., Fisher, J. B., Worden, J., Jones, D. B. A., Berry, J., Collatz, G. J., Baker, I. T., Jung, M., Liu, J., Osterman, G., O'Dell, C., Sparks, A., Butz, A., Guerlet, S., Yoshida, Y., Chen, H., and Gerbig, C.: Interpreting seasonal changes in the carbon balance of southern Amazonia using measurements of XCO₂ and chlorophyll fluorescence from GOSAT, *Geophys. Res. Lett.*, 40, 2829–2833, <https://doi.org/10.1002/grl.50452>, 2013.
- Peters, W., Jacobson, A. R., Sweeney, C., Andrews, A. E., Conway, T. J., Masarie, K., Miller, J. B., Bruhwiler, L. M. P., Pétron, G., Hirsch, A. I., Worthy, D. E. J., van der Werf, G. R., Randerson, J. T., Wennberg, P. O., Krol, M. C., and Tans, P. P.: An atmospheric perspective on North American carbon dioxide exchange: CarbonTracker, *P. Natl. Acad. Sci. USA*, 104, 18925–18930, <https://doi.org/10.1073/pnas.0708986104>, 2007.
- Phillips, D. L.: A Technique for the Numerical Solution of Certain Integral Equations of the First Kind, *J. ACM*, 9, 84–97, <https://doi.org/10.1145/321105.321114>, 1962.
- Reuter, M., Buchwitz, M., Schneising, O., Krautwurst, S., O'Dell, C. W., Richter, A., Bovensmann, H., and Burrows, J. P.: Towards monitoring localized CO₂ emissions from space: co-located regional CO₂ and NO₂ enhancements observed by the OCO-2 and S5P satellites, *Atmos. Chem. Phys.*, 19, 9371–9383, <https://doi.org/10.5194/acp-19-9371-2019>, 2019.
- Rodgers, C.: *Inverse Methods for Atmospheric Sounding: Theory and Practice*, World Scientific, Singapore, 2000.
- Sandau, R. (Ed.): *Digital Airborne Camera: Introduction and Technology*, Springer Science & Business Media B.V., <https://doi.org/10.1007/978-1-4020-8878-0>, 2010.
- Schaaf, C. B., Gao, F., Strahler, A. H., Lucht, W., Li, X., Tsang, T., Strugnell, N. C., Zhang, X., Jin, Y., Muller, J.-P., Lewis, P., Barnsley, M., Hobson, P., Disney, M., Roberts, G., Dunderdale, M., Doll, C., d'Entremont, R. P., Hu, B., Liang, S., Privette, J. L., and Roy, D.: First operational BRDF, albedo nadir reflectance products from MODIS, *Remote Sens. Environ.*, 83, 135–148, [https://doi.org/10.1016/S0034-4257\(02\)00091-3](https://doi.org/10.1016/S0034-4257(02)00091-3), 2002.
- Schepers, D., aan de Brugh, J., Hahne, P., Butz, A., Hasekamp, O., and Landgraf, J.: LINTRAN v2.0: A linearised vector radiative transfer model for efficient simulation of satellite-born nadir-viewing reflection measurements of cloudy atmospheres, *J. Quant. Spectrosc. Ra.*, 149, 347–359, <https://doi.org/10.1016/j.jqsrt.2014.08.019>, 2014.
- Schwandner, F. M., Gunson, M. R., Miller, C. E., Carn, S. A., Eldering, A., Krings, T., Verhulst, K. R., Schimel, D. S., Nguyen, H. M., Crisp, D., O'Dell, C. W., Osterman, G. B., Iraci, L. T., and Podolske, J. R.: Spaceborne detection of localized carbon dioxide sources, *Science*, 358, 6360, <https://doi.org/10.1126/science.aam5782>, 2017.
- Stier, P., Feichter, J., Kinne, S., Kloster, S., Vignati, E., Wilson, J., Ganzeveld, L., Tegen, I., Werner, M., Balkanski, Y., Schulz, M., Boucher, O., Minikin, A., and Petzold, A.: The aerosol-climate model ECHAM5-HAM, *Atmos. Chem. Phys.*, 5, 1125–1156, <https://doi.org/10.5194/acp-5-1125-2005>, 2005.
- Thompson, D. R., Leifer, I., Bovensmann, H., Eastwood, M., Fladelland, M., Frankenberg, C., Gerilowski, K., Green, R. O., Kratwurst, S., Krings, T., Luna, B., and Thorpe, A. K.: Real-time remote detection and measurement for airborne imaging spectroscopy: a case study with methane, *Atmos. Meas. Tech.*, 8, 4383–4397, <https://doi.org/10.5194/amt-8-4383-2015>, 2015.
- Thompson, D. R., Thorpe, A. K., Frankenberg, C., Green, R. O., Duren, R., Guanter, L., Hollstein, A., Middleton, E., Ong, L., and Ungar, S.: Space-based remote imaging spectroscopy of the

- Aliso Canyon CH₄ superemitter, *Geophys. Res. Lett.*, 43, 6571–6578, <https://doi.org/10.1002/2016GL069079>, 2016.
- Thorpe, A., Frankenberg, C., Aubrey, A., Roberts, D., Nottrott, A., Rahn, T., Sauer, J., Dubey, M., Costigan, K., Arata, C., Stefke, A., Hills, S., Haselwimmer, C., Charlesworth, D., Funk, C., Green, R., Lundeen, S., Boardman, J., Eastwood, M., Sarture, C., Nolte, S., Mccubbin, I., Thompson, D., and McFadden, J.: Mapping methane concentrations from a controlled release experiment using the next generation airborne visible/infrared imaging spectrometer (AVIRIS-NG), *Remote Sens. Environ.*, 179, 104–115, <https://doi.org/10.1016/j.rse.2016.03.032>, 2016.
- Thorpe, A. K., Frankenberg, C., and Roberts, D. A.: Retrieval techniques for airborne imaging of methane concentrations using high spatial and moderate spectral resolution: application to AVIRIS, *Atmos. Meas. Tech.*, 7, 491–506, <https://doi.org/10.5194/amt-7-491-2014>, 2014.
- Thorpe, A. K., Frankenberg, C., Green, R. O., Thompson, D. R., Aubrey, A. D., Mouroulis, P., Eastwood, M. L., and Matheou, G.: The Airborne Methane Plume Spectrometer (AMPS): Quantitative imaging of methane plumes in real time, in: 2016 IEEE Aerospace Conference, pp. 1–14, <https://doi.org/10.1109/AERO.2016.7500756>, 2016.
- Thorpe, A. K., Frankenberg, C., Thompson, D. R., Duren, R. M., Aubrey, A. D., Bue, B. D., Green, R. O., Gerilowski, K., Krings, T., Borchardt, J., Kort, E. A., Sweeney, C., Conley, S., Roberts, D. A., and Dennison, P. E.: Airborne DOAS retrievals of methane, carbon dioxide, and water vapor concentrations at high spatial resolution: application to AVIRIS-NG, *Atmos. Meas. Tech.*, 10, 3833–3850, <https://doi.org/10.5194/amt-10-3833-2017>, 2017.
- Tikhonov, A.: On the solution of incorrectly stated problems and method of regularization, *Dokl. Akad. Nauk. SSSR*, 151, 501–504, 1963.
- Ummel, K.: CARMA Revisited: An Updated Database of Carbon Dioxide Emissions From Power Plants Worldwide, Center for Global Development, Working Paper 304, 2012.
- Varon, D. J., Jacob, D. J., McKeever, J., Jervis, D., Durak, B. O. A., Xia, Y., and Huang, Y.: Quantifying methane point sources from fine-scale satellite observations of atmospheric methane plumes, *Atmos. Meas. Tech.*, 11, 5673–5686, <https://doi.org/10.5194/amt-11-5673-2018>, 2018.
- Varon, D., McKeever, J., Jervis, D., Maasackers, J., Pandey, S., Houweling, S., Aben, I., Scarpelli, T., and Jacob, D.: Satellite discovery of anomalously large methane point sources from oil/gas production, *Geophys. Res. Lett.*, 46, 22, <https://doi.org/10.1029/2019GL083798>, 2019.
- Wheeler, D. and Ummel, K.: Calculating CARMA: global estimation of CO₂ emissions from the power sector, Center for Global Development, Working Paper 145, 2008.
- Wilzewski, J. S., Roiger, A., Strandgren, J., Landgraf, J., Feist, D. G., Velazco, V. A., Deutscher, N. M., Morino, I., Ohyama, H., Té, Y., Kivi, R., Warneke, T., Notholt, J., Dubey, M., Sussmann, R., Rettinger, M., Hase, F., Shiomi, K., and Butz, A.: Spectral sizing of a coarse-spectral-resolution satellite sensor for XCO₂, *Atmos. Meas. Tech.*, 13, 731–745, <https://doi.org/10.5194/amt-13-731-2020>, 2020.